Multibody System Dynamics manuscript No.
(will be inserted by the editor)

Optimal Design of Active-Passive Shoulder Exoskeletons: A Computational Modeling of Human-Robot Interaction

Ali Nasr · Sydney Bell · John McPhee

Received: 11.05.2022 / Accepted: 01.11.2022

Abstract Exoskeleton robots, which range from fully passive to fully active-assisted movements, have become an essential instrument for assisting industrial employees and stroke rehabilitation therapy. Designing the exoskeleton actuation is challenging and time-consuming due to closed-kinematic loops in the 3D human-exoskeleton multibody model, complicated interactions, and interdependent selection of power transmission features. This research proposes a process for dynamic syntheses of passive and active assistive shoulder exoskeletons. Firstly, a multibody model was developed using six components: an upper-body musculoskeletal model, an optimal controller, the exoskeleton's rigid body, a passive mechanism, a powered actuator, and an assistance model. The desired motion was experimentally measured from six tasks: frontal reaching, left to right reaching, overhead reaching, sagittal-plane object handling, frontal-plane object handling, and over-head object handling. The system design was optimized by choosing features of the passive mechanism and exoskeleton motor such that the human joint active torque, power, muscle metabolic energy expenditure, and actuator electricity consumption were minimized. The dynamic synthesis processes were found to be successful, and the resultant optimized active-passive exoskeletons allow for the creation of lighter and smaller wearable robots that reduce the user's muscular activation torque for the tasks being studied.

Keywords wearable robots · exoskeletons · active-passive · closed kinematic chain · human-robot interaction · assistive control

1 Introduction

Work-related musculoskeletal diseases (MSDs) affecting the upper extremities, particularly the shoulders, are widespread among Canadian workers [1–5]. The shoulder's complex design makes it vulnerable to damage, overexertion, repetitive motion, and large anteversion angles are additional well-known exposures that contribute to work-related MSDs [4, 6, 7]. Increased injury risk and MSD at the shoulder are significantly linked to accumulative exposure to overhead postures and shoulder joint elevation exceeding more than 60 degrees [4, 8]. Specifically, the subacromial space narrows as the arm is elevated, and when the shoulder muscles fatigue, their capability to preserve the humeral head in the glenohumeral cavity decreases. This further decreases the subacromial space and increases the risk of supraspinatus tendon tears or impingement [8]. Shoulder injury occurs as a result of persistent high muscular activation (which can lead to muscle fatigue and overuse injury) and the subsequent increased internal (joint) force/torque (which can cause acute or chronic joint pain and injury) [6–9]. From a financial viewpoint, in one US state, the total medical and insurance cost of all shoulder MSDs claims was projected to be $457 M with more than 7 days of lost work over 5 years [10]. The requirements for upper extremities assistance are increasing in various sectors, including reducing worker effort stresses or supporting and rehabilitating patients with neuromuscular impairments [4, 11].

Recently, the exoskeleton is one solution that has sparked attention in the scientific and industrial worlds [12–15]. Wearable exoskeletons help boost human performance, aiding human motions to minimize the user's effort, and decreasing fatigue. Exoskeletons, therefore, contribute to lowering the risk of work-related MSDs, and can also be applied to patients recovering or developing motor skills [7, 9, 11–13, 15].

A. Nasr
E-mail: a.nasr@uwaterloo.ca
Department of Systems Design Engineering, University of Waterloo, Waterloo, ON, Canada

The design of a functional exoskeleton should be compact, lightweight, user-friendly, and have no intrusive influence on the user [16, 17]. These requirements support the employment of optimization steps in system design, configuration, and manufacturing [15, 17–19]. The exoskeleton design splits into three categories based on sources of assistance: fully passive, fully active, and active-passive.

Passive exoskeletons are equipped with a mechanism to store potential energy from human motion for future use [12, 20]. For example, upper limb passive exoskeletons are mostly meant to unload the weight of the arm and any lifted tool while the arm is elevated, decreasing muscular strain [13]. The mechanism is assembled from a spring [19, 20], an elastic band [21], a counterweight [18, 22], or composed of a pneumatic cylinder for gravity compensation [23, 24]. The main advantages of entirely passive exoskeletons include being lightweight, portable, safe, affordable, high power-to-weight, less complex concerning sensing and control, and requiring less maintenance than other categories [12, 16, 20, 25, 26]. Consequently, a significant interest in studying, developing, commercializing, and utilizing passive industrial exoskeletons does exist [12, 13, 27]. On the other hand, passive devices are limited to providing a consistent torque profile for gravity-concerned movements only [11, 12, 20, 28]. However, the user may exert even more effort with a passive exoskeleton than without for some problematic dynamic activities [29].

On the contrary, active (powered) exoskeletons supply an assistive torque through a flexible function of time instead of the constant function of joint angle [12, 15, 20]. The assistive force/torque is achieved through a controllable component such as an electric motor, a hydraulic cylinder, or a pneumatic artificial muscle [26, 30, 31]. This actuator controls via a sophisticated control algorithm that requires various types of sensors and energy sources [15, 23, 30–36]. Since the total torque source relies on an active component, the utilized actuator and the energy source should be powerful and, consequently, are bulky, heavy, irremovable, expensive, and have a lower power-to-weight ratio (PWR) [27]. Increased device bulk and inertia resulting from heavier motors and battery packages would necessitate more effort from the human body, lowering motion efficiency through increased metabolic power use [37].

To mitigate the issues of active and passive exoskeletons, some devices use a combination of active and passive power transmissions [18, 38–42]. Essentially, passive mechanisms contribute to lowering the size, weight, and required active torque, advancing the portability [11, 18, 43]. The motor primarily provides extra assistance and may be used in negative work harvesting like electric vehicles [44, 45]. Specifically, the operating time of an active exoskeleton robot can be increased by more than 20% thanks to an energy harvesting module [45]. Recently, this combination transmission system has been conceptually studied as semi-active, semi-passive, or quasi-passive on lower-limb [9, 23, 38, 39, 45–48], upper-limb [19, 41, 43, 49, 50], and spinal [32] wearable robots. Using the combined systems (especially the rotational inertia) may decrease the angular velocity and acceleration of the user by more than 60% [50]. Controlling the active component of this combined system requires considering the interaction with the human [33], the motor control (activation) delay [18], and understanding the dynamics of both systems. We aim to evaluate a fully passive, fully active, and active-passive shoulder exoskeleton and compare them for the specific task.

Designing the power transmission source for an exoskeleton requires a deep understanding and broad consideration of both human and robot systems via different criteria. In designing exoskeletons, several research studies employed multibody dynamic models of human limbs that are kinematically constrained to the exoskeletons' structure [20, 51]. Regarding the redundant actuation in these multibody human-exoskeleton models, various cost functions were optimized in the designing process [11, 13, 20]. These optimization variables are classified into (I) kinematic, (II) dynamic, and (III) biomechanics parameters.

Examples of the kinematic variables in the optimization are the dimensions of the exoskeleton and the kinematic fit to subjects via geometric parameters [52], the linkage dimensions of the exoskeleton to maximize the force transmission to the wearer [53], or motion/task-based optimization [54, 55]. The dynamic parameter optimization for active exoskeletons are motor torques, or for passive exoskeletons are the characteristics of the spring within the passive mechanism [11]. In this scenario, the optimization goal was to reduce human effort in the form of joint (cumulative and peak) torques [7, 20, 56, 57], powers [7, 58], joint reaction force [59], and muscle forces [7, 60]. An example of a biomechanics parameter in optimization is muscle fatigue, which is reduced [9, 19, 61] or, specifically, muscle activity measured through electromyography [9, 38, 46, 48]. We aim to design the system by concerning human variables (e.g., joint torque, active torque, activation signal, and power) and robot properties (e.g., the power, the inertia, and the dimensions of the actuator).

The model-based optimization utilizes a dynamic model expressed by nonlinear problems using forward dynamics simulations of the multibody human-exoskeleton model [60] and an optimal controller as the human central nervous system (CNS) [62]. Note that the exoskeleton's controller is introduced in section 3.2.5. The forward and inverse dynamic simulations utilize two equations classifications according to exoskeletons' joints/axis configuration and requirements. The first classification is the ordinary differential equation (ODE) that are used for multibody models in which the exoskeleton joints/axis coincide with the human joints [51]. The exoskeleton link can be grouped with human segmental bodies and simplify the multibody model [51]. The second classification is the differential algebraic equations (DAEs) that are used

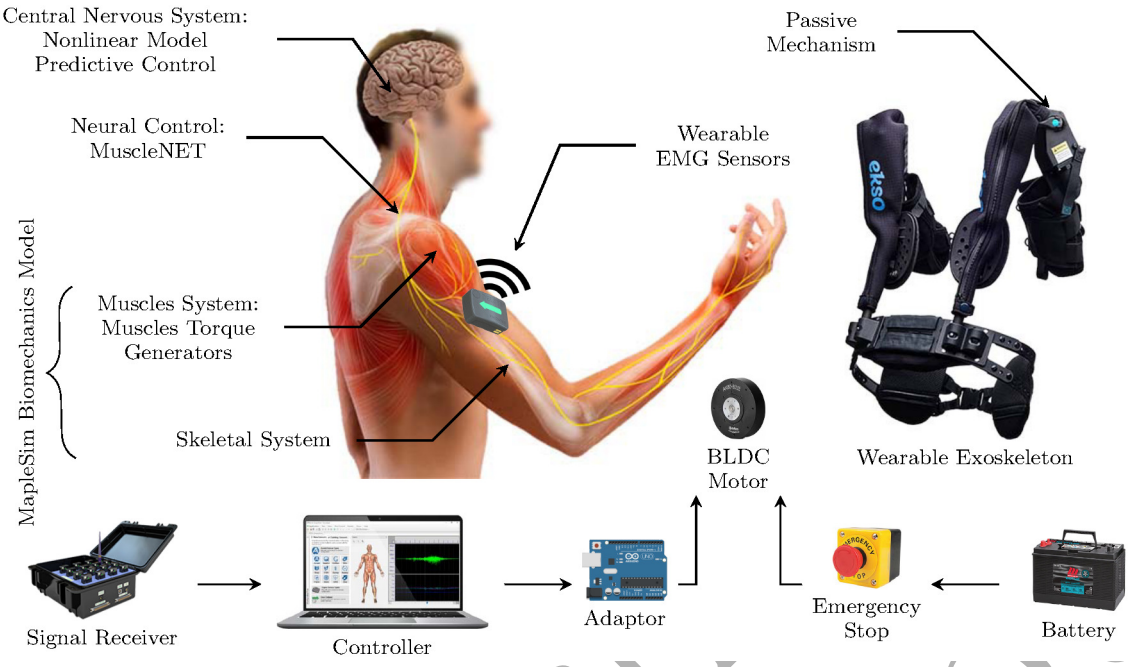

Fig. 1: The essential components of the human-robot system. The human consists of the CNS (modeled using NMPC [62]), neural control (previously modeled by MuscleNET [67, 68]), muscle (modeled using the MTGs of human model), and skeletal system. The robot consists of mechanical and electrical hardware. The essential electrical components are wearable wireless surface electromyography (sEMG) sensors and the receiver (Delsys Inc, Boston, MA), controller, adaptor, BLDC motor, emergency stop, and battery. The EVO (Ekso Bionics Holdings Inc, California, USA) upper limb exoskeleton is used as a wearable device with three levels of passive assistance.

for the multibody system with misaligned human-exoskeleton respective joints (primarily for higher than 1-degree of freedom (DoF) joints, for example, 3-DoF shoulder joints) [11, 20, 63, 64]. Using DAE instead of ODE can provide the opportunity to measure and evaluate human-robot interaction forces/torques. Due to the formed closed-loop kinematic chains in the multibody human-exoskeleton model, the governing equations are DAEs within additional interaction dynamic and the kinematic constraints model than the motion equation [11, 20, 65, 66]. However, solving the DAEs is challenging, time-consuming, and not straightforward. We aim to introduce the framework for designing exoskeletons using DAEs.

To the best of our knowledge, the literature has not supplied clear guidelines to design and optimization of complex fully passive, fully active, and active-passive systems alongside using a complicated human-exoskeleton interaction model. First and foremost, this research aims to create dynamic analysis techniques that may be used to construct and customize an upper limb exoskeleton for a specific worker or patient. The second objective is to decrease the user's effort by choosing motor and passive element characteristics. For task-based designing and optimization, the data were recorded from participants doing functional activities.

The list of the research's contributions is as follows:

i. Modeled the human-exoskeleton multibody system (using six components: the MapleSim Biomechanics upper-body dynamic model (consist of 20 DoF and 40 muscle torque generators (MTGs)), a nonlinear model predictive control (NMPC), the exoskeleton's rigid body, a passive mechanism, a powered actuator (brushless direct current (BLDC) motor), and an assist-as-needed (AAN) model) and used DAEs simulation to study the interaction force/torque.
ii. Proposed a guideline to design fully active, fully passive, and active-passive transmission system components.
iii. Optimized the actuation properties using multiple criteria such as the human joint variables and signals as well as practical manufacturing criteria, including the power, inertia, and dimension of the actuator.
iv. Proposed a model of integrating passive mechanisms with motors that leads to smaller and more lightweight motor selection (Figure 1).

First, the six recorded industrial tasks or motions were introduced in section 2. Second, a multibody human-exoskeleton dynamic model was developed and discussed in section 3 using a couple of independent subcomponents models. Third, the design variable, targeted cost function, the procedure of actuator

designing, and the model-based optimization method are introduced (section 4). Finally, the results for different tasks, cost functions, and actuators are presented and discussed.

2 Data acquisition and processing

2.1 Tasks

Occupational tasks are generally used for evaluating the efficient design of industrial exoskeletons that reduce muscular demands [13]. For example, overhead work and carrying a heavy load can be a challenging risk to eliminate in specific industries, such as automotive production and hand assembly [13]. So far, a couple of industrial and daily living tasks are used for evaluating upper limb exoskeletons, such as (1) overhead raising, maintaining, operating, and moving [8, 42, 69–72], (2) lifting a load from the ground and transferring [73, 74], (3) general raising, reaching, and lowering arms [11, 61], (4) static holding in stooped posture [41, 73], (5) plugging needle into holes and groove [75], (6) surgery operation simulation [76], (7) daily living tasks (e.g., eating with a spoon, opening a door, zipping a coat, and combing hair) [11]. Six tasks were designed to simulate industrial and daily activities to guarantee that each joint had a wide range of amplitudes. As depicted in Figure 2, tasks are categorized into two groups: arm moving and object handling. The tasks are frontal reaching, left to right reaching, overhead reaching, sagittal-plane object handling, frontal-plane object handling, and over-head object handling.

2.2 Data recording

One volunteer (male, age: 29 years; mass: 76 kg; height: 1.80 m; right-handed; 1 session workout per week), free of upper limb injury, provided informed consent and was recruited for this study. The experimental protocol followed the Declaration of Helsinki's guidelines. The University of Waterloo's Office of Research Ethics approved the data collecting study (ORE #: 31194).

An MVN Suit (Xsens Technologies, Netherlands) based on the inertial measurement unit (IMU) technology was used to quantify the angular human joint kinematics (without exoskeleton). The subject conducted tasks with 2 minutes of rest between tasks after a standard calibration of the IMU system. The data were captured at a rate of 100 Hz.

2.3 Kinematic process

Similar to the kinematic process used [20, 77], the following steps were applied to filter the joint angles and estimate the joint angular velocity, acceleration, and the raising and lowering of the object.The processed kinematic data were used as the reference trajectory in section 4.1.

A 10 Hz low-pass filter was used to ignore the high-frequency noises. Then, the position data were re-sampled with a rate of 50 Hz using 1-D data cubic interpolation of the neighboring values. The velocity and acceleration of the joints were initially calculated using the numerical first and second derivatives of joint angles. Then, with a cut-off frequency of 20 and 30 Hz, two low-pass second-order Butterworth filters were used to ignore minor variations.

The object's position and velocity were used to distinguish the raising and lowering processes. The object was estimated at the resting targets when the absolute velocity of the object was less than 1 cm/s for more than 30 milliseconds.

3 Multibody system model

As shown in Figure 3, the multibody model consists of two sub-models of the human (section 3.1) and the exoskeleton (section 3.2). More details on the connection of these systems are described in section 3.3. The multibody system was modeled using MapleSim v2021 (Maplesoft, Waterloo, ON, Canada), a multibody dynamic system modeling and simulation software package, and exported as symbolic optimized C code to MATLAB (R2021b. MathWorks, Natick, MA, USA) for use in the design and optimization process.

3.1 Human model

The human body model and the CNS control loop are introduced in this section.

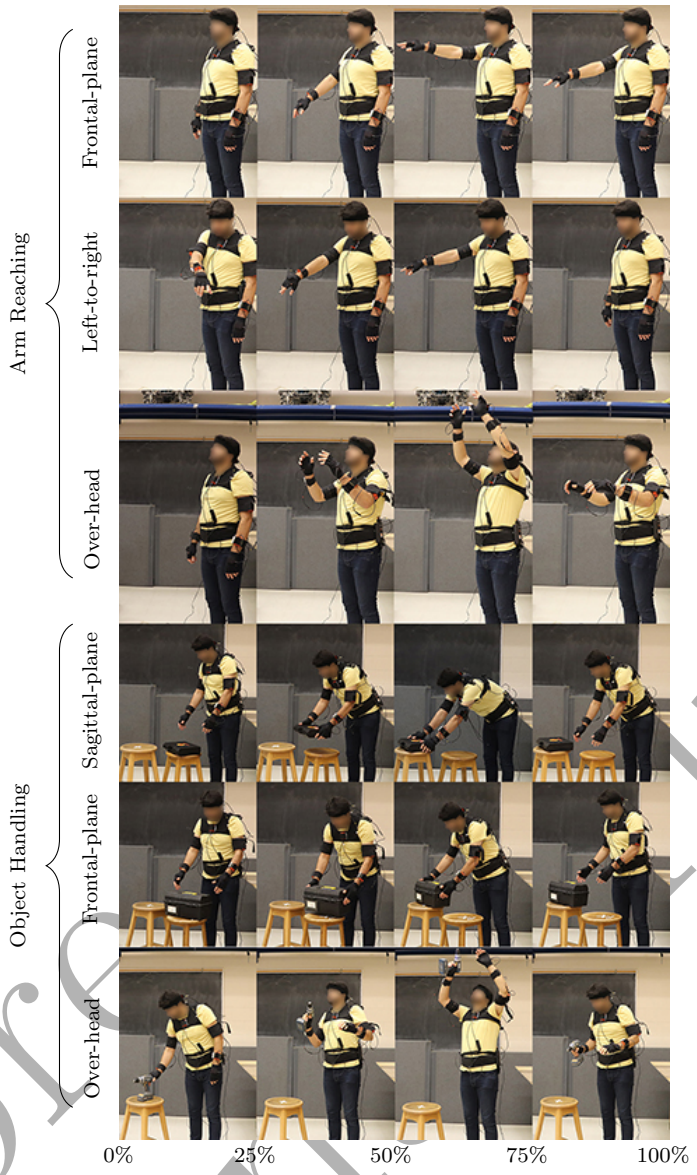

Fig. 2: Illustration of six industrial and daily living activity tasks for designing, optimizing, and evaluating the shoulder exoskeleton. The first three motions are arm-reaching tasks, and the last three motions are object-handling tasks.

3.1.1 Upper-body dynamic model

The MapleSim Biomechanics (scalable musculoskeletal (MSK)) model developed and validated using experimental dynamometer data for dynamic simulations of movement was used for the upper body. The MapleSim Biomechanics upper body model is comprised of 8 body segments (torso, head, left/right upper arm, left/right forearm, and left/right hand) and has 20 DoF. The MapleSim Biomechanics model has two components of a skeletal dynamic and biomechanical joint torque model. The biomechanical joint torque model is developed with MTGs [78] that consists of 6 functions of (I) the passive torque, (II) peak joint strength, (III) active-torque-angle scaling, (IV) active-torque-angular-velocity scaling, and (V) excitation-to-activation signal. The MTG parameter values were identified for the simulated subject using a dynamometer device in isometric, isokinetic, and passive modes [33, 78]. The MapleSim Biomechanics model can be adjusted for various anthropometric measurements and body characteristics, including sex, age, body mass, height, dominant side, and physical activity. The adjustable MapleSim Biomechanics model allows for the evaluation of the exoskeleton on different subjects. There are 3 joints at torso (torso flexion/extension (TFE), torso right/left lateral flexion (TRLLF), and torso right/left axial rotation (TRLAR)), and 3 joints at neck (neck flexion/extension (NFE), neck right/left lateral flexion (NRLLF), and neck right/left axial rotation (NRLAR)). For each side of the body, there are 3 DoF at shoulder joint

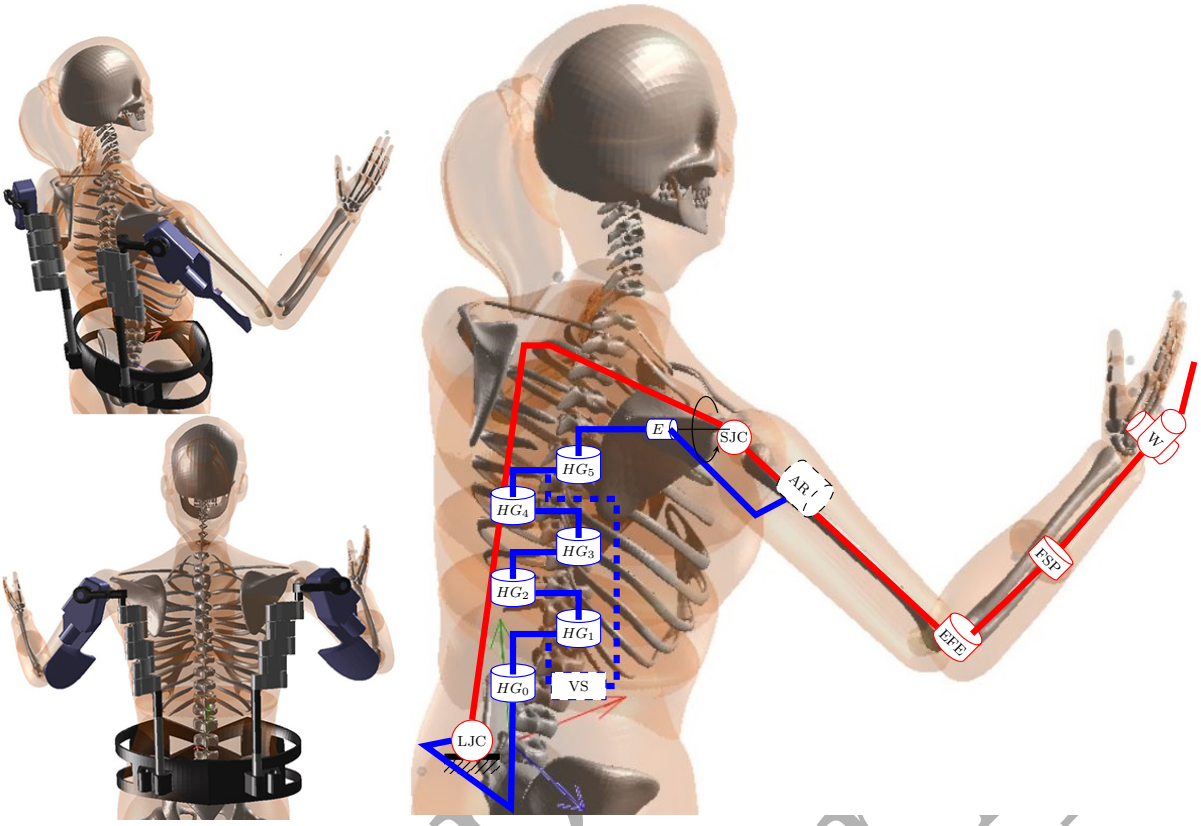

(a) EVO with MapleSim Biomechanics (b) The human-exoskeleton closed kinematic chain

Fig. 3: (a) Two views of 20-DoF MapleSim Biomechanics model of a human upper body and EVO upper limb exoskeleton. The essential human joints are the lumbar joint center (LJC) with a 3-DoF spherical joint (TFE, TRLLF, and TRLAR), SJC with a 3-DoF spherical joint (SFE, SAA, and SMLR), EFE, FPS, a 2-DoF wrist joint (WFE, and WRUD). (b) Schematic diagram of the human and exoskeleton closed kinematic loop models and their interaction with hinge (HG), elevation (E), and virtual spring (VS) joints. The human and exoskeleton systems are connected at the armrest (AR) and LJC.

centre (SJC) (shoulder flexion/extension (SFE), shoulder adduction/abduction (SAA), and shoulder medial/lateral rotation (SMLR)), elbow flexion/extension (EFE), forearm pronation/supination (FPS), wrist flexion/extension (WFE), and wrist radial/ulnar deviation (WRUD).

The MapleSim Biomechanics dynamic model is presented as Equation (1). For the active-torque-driven model, Equation (3) is used instead of Equation (2) which is for the excitation-signal-driven model. Note that Equations (1-3) are only for the human body and the combined human-exoskeleton model is provided in Equations (18-20).

$$\begin{bmatrix} I_{2n\times 2n} & 0 \\ 0 & \mathbf{M}_{n\times n}\left(\boldsymbol{\theta}_{n\times 1},\beta\right) \end{bmatrix} \begin{bmatrix} \dot{\boldsymbol{a}}_{2n\times 1} \\ \dot{\boldsymbol{\omega}}_{n\times 1} \end{bmatrix} = \begin{bmatrix} \dot{\boldsymbol{\tau}}_{u2a}\left(\boldsymbol{a}_{2n\times 1},\boldsymbol{u}_{2n\times 1},t,\beta\right)_{2n\times 1} \\ \mathbf{F}_{n\times 1}\left(\boldsymbol{\omega}_{n\times 1},\boldsymbol{\theta}_{n\times 1},\beta\right)+\mathbf{Q}_{n\times 1} \end{bmatrix} \tag{1}$$

$$\mathbf{Q}_{n\times 1} = \left[\boldsymbol{a}^{+}\boldsymbol{\tau}_{\omega}^{+}\left(\boldsymbol{\omega},\beta\right)\boldsymbol{\tau}_{\theta}^{+}\left(\boldsymbol{\theta},\beta\right)\boldsymbol{\tau}_{0}^{+}\left(\beta\right)+\boldsymbol{a}^{-}\boldsymbol{\tau}_{\omega}^{-}\left(\boldsymbol{\omega},\beta\right)\boldsymbol{\tau}_{\theta}^{-}\left(\boldsymbol{\theta},\beta\right)\boldsymbol{\tau}_{0}^{-}\left(\beta\right)+\boldsymbol{\tau}_{p}\left(\boldsymbol{\theta},\boldsymbol{\omega},\beta\right)\right]_{n\times 1} \tag{2}$$

$$\mathbf{Q}_{n\times 1} = \left[\boldsymbol{\tau}_{a}+\boldsymbol{\tau}_{p}\left(\boldsymbol{\theta},\boldsymbol{\omega},\beta\right)\right]_{n\times 1} \tag{3}$$

where

n	the number of independent coordinates and speeds
$\boldsymbol{\theta}$	the column matrix of all joint angles
$\boldsymbol{\omega}$	the column matrix of all joint angular speed
$\mathbf{M}$	the mass matrix
$\mathbf{F}$	the segments' Coriolis, centrifugal, and gravitational effects
$\mathbf{Q}$	the applied joint torques, a column matrix containing $\tau_h\left(t\right)$ for all joints
$\boldsymbol{\tau}_{u2a}$	the excitation-to-activation signal ODE function

$\boldsymbol{\tau}_{\omega}$	the active torque-angular-velocity scaling function
$\boldsymbol{\tau}_{\theta}$	the active torque-position scaling function
$\boldsymbol{\tau}_0$	the peak isometric joint strength
$\boldsymbol{\tau}_p$	the passive torque function due to viscous damping and nonlinear stiffness
$\boldsymbol{\tau}_a$	the vector containing the active torques at the joints
$^+$	the positive direction of joint
$^-$	the negative direction of the joint
β	the subject adjustment variables: sex, age, body mass, height, dominant side, and physical activity

3.1.2 Optimal controller model of the CNS

The CNS is in charge of the motion of the human body [62, 79]. The CNS synchronizes the kinetics and kinematics regardless of complex MSK dynamics and unknown/uncertain disturbances and trajectories [79]. Human mobility studies suggest that the CNS coordinates body movements based on optimization [80].

The CNS uses a complicated command to coordinate human motions, composed of two sectors: motion prediction and correction command [62]. To compute motion prediction (model-based feed-forward control), an internal model (IM) as a representation of the complicated system is used. Furthermore, the sensory organs calculate a correction instruction or feedback control to correct any errors caused by model uncertainty, external disruption, or a new environment. NMPC with a short time horizon is shown to be able to attain this multi-purpose control complexity (feed-forward and feedback control) [62]. Precisely, to simulate human dynamics, the NMPC uses an IM that is learned, identified, and tuned over time [81] to forecast optimal motion (feed-forward) and correct prediction errors (feedback) [62]. It uses a cost function to evaluate the ideal motion. Here, we construct this cost function with biomechanical variables such as joint angles and velocity errors, as well as model inputs and their derivative. This cost function is similar to Equation (4) for the active-torque-driven model. NMPC controller optimizes the cost functional (Equation (4)) under the impact of system dynamics (section 3.3.2) and limitations (Equation (5)).

$$J_{CNS} = \int_0^{t_f} \left[\mathbf{W}_1^T \left(\boldsymbol{\theta} - \boldsymbol{\theta}_d\right)^2 + \mathbf{W}_2^T \left(\boldsymbol{\omega} - \boldsymbol{\omega}_d\right)^2 + \mathbf{W}_3^T \left(\boldsymbol{\tau}_a\right)^2 + \mathbf{W}_4^T \left(\dot{\boldsymbol{\tau}}_a\right)^2 \right] dt \tag{4}$$

$$\begin{gathered} \boldsymbol{\theta}_{min}\left(\beta\right) \leq \boldsymbol{\theta} \leq \boldsymbol{\theta}_{max}\left(\beta\right) \\ \boldsymbol{\omega}_{min}\left(\beta\right) \leq \boldsymbol{\omega} \leq \boldsymbol{\omega}_{max}\left(\beta\right) \\ -R\boldsymbol{\tau}_0^-\left(\beta\right) \leq \boldsymbol{\tau}_a \leq R\boldsymbol{\tau}_0^+\left(\beta\right) \\ \dot{\boldsymbol{\tau}}_{min} \leq \dot{\boldsymbol{\tau}}_a \leq \dot{\boldsymbol{\tau}}_{max} \end{gathered} \tag{5}$$

where

$\mathbf{W}$	the vector of cost function weights
$\boldsymbol{\theta}$	the vector containing the joint angles
$\boldsymbol{\omega}$	the vector containing the joint instantaneous angular velocities
$\boldsymbol{\tau}_a$	the vector containing the active torques at the joints
$\dot{\boldsymbol{\tau}}_a$	the vector containing the instantaneous active torque rates at the joints
$\boldsymbol{\tau}_0$	the peak isometric joint strength
R	the ratio of the maximum eccentric isokinetic torque over the maximum isometric torque
t_f	the prediction horizon
d	the desire value or trajectory, recorded in section 2.2 and processed in section 2.3
min	the minimum variable
max	the maximum variable
$^+$	the positive direction of joint
$^-$	the negative direction of the joint
β	the subject adjustment variables: sex, age, body mass, height, dominant side, and physical activity

The cost function weights were selected for long-term experience and robust trajectory tracking according to the study in [33]. The IM is the human model mentioned in section 3.1.1. In addition, the NMPC has full awareness of the interaction force/torque of the exoskeleton and the external force/torque of the manipulated object.

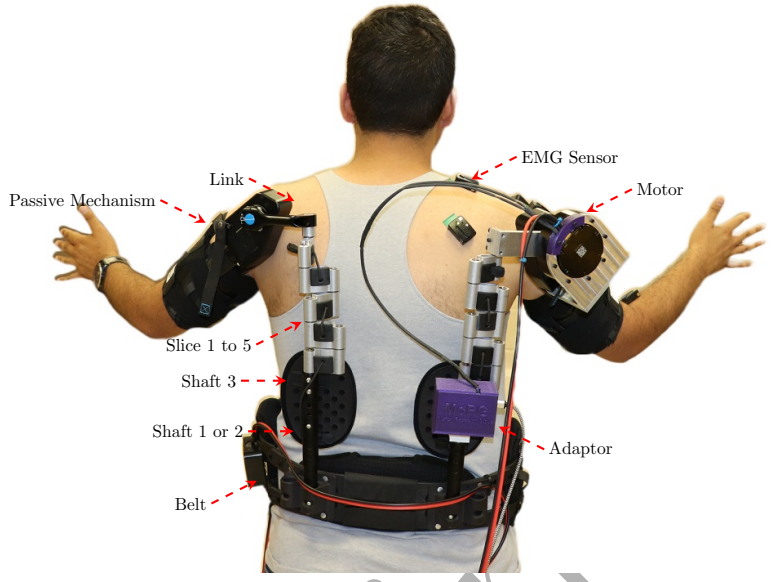

Fig. 4: An image of the actual active-passive shoulder exoskeleton. The important mechanical parts (e.g., belt, shafts, slices, link, and mechanism) and the electrical components (e.g., adaptor, motor, and sEMG sensor) are shown in the image.

Table 1: The coordinates location, mass, COM, and inertia matrix of the mechanical system's links (the right tower of the exoskeleton).

#	Part Name	Coordinate		Center of Mass (m)	Mass (kg)	Inertia Matrix (kgm2)					
		Parent	Child			I_{xx}	I_{yy}	I_{zz}	I_{xy}	I_{xz}	I_{yz}
P1	Belt	LJC	RH1: -0.063, 0.000, 0.135 RH2: -0.067, 0.000, 0.100	0.059, 0.000, 0.000	0.711	0.01	0.017	0.008	-4e-6	0	0
P21	Shaft 1	H	L1: 0.000, 0.145, 0.000	0.000, 0.072, 0.000	0.036	64e-6	3e-6	64e-6	0	0	0
P22	Shaft 2	H	L2: 0.000, 0.220, 0.000	0.000, 0.110, 0.000	0.052	210e-6	3e-6	210e-6	0	0	0
P3	Shaft 3	L	HG0: 0.000, 0.133, 0.000	0.000, 0.071, 0.000	0.031	50e-6	2e-6	50e-6	0	0	0
P4-P8	Slice	HG	HG1: 0.000, 0.036, 0.057	0.000, 0.016, 0.030	0.075	50e-6	46e-6	9e-6	0	0	-1e-6
P9	Link	HG5	E: -0.018, 0.024, 0.080	-0.011, 0.022, 0.040	0.083	116e-6	118e-6	13e-6	1e-6	21e-6	-5e-6
P10	Mechanism	E	AR: 0.126, -0.170, 0.000	0.049, -0.072, -0.020	0.850	0.005	0.001	0.006	0.002	433e-6	-0.001

3.2 Exoskeleton model

Here, the rigid links, the joint configuration, the passive torque, and the active torque of the exoskeleton model are described. The topology and kinematic structure of the exoskeleton are already shown on Figure 3b and highlighted in the Figure 4 for further consideration.

3.2.1 Dimensions and inertia properties

We used an EVO (Ekso Bionics Holdings Inc, California, USA) upper limb exoskeleton as the wearable device with passive assistance. However, the described method can be applied to any upper-limb exoskeleton. All robot linkages were reverse-engineered utilizing a mixture of physical measurements and reference photos available from the manufacturer to create computer-aided geometric models. A digital caliper, tape meter, and scale were used to measure the dimension of each link, the joint center locations, and the mass of the robot. The center mass and inertia matrix were calculated using the design software with the assumption that the part has constant density. The joint attachment coordinates, the center of mass (COM), mass, and inertia matrix are provided in Table 1.

3.2.2 Joints configuration

The exoskeleton has 2 adjustment links and 7 joints that form a tower on each side. Here, the adjustment options and the joints of the exoskeleton are described. The exoskeleton-human attachment, interaction, and closed-kinematic loop are described in section 3.3.1.

Table 2: The hinge's passive joint parameters for the right tower of the exoskeleton.

Joint	K (Nm/rad)	φ_0 (rad)	k_1 (Nm)	k_2 (1/rad)	k_3 (Nm)	k_4 (1/rad)	$\varphi^-_{\max}$ (rad)	$\varphi^+_{\max}$ (rad)	c (Nms/rad)
HG0	0.1	0	1	10	1	10	0	$-\pi$	0.001
HG1	0.1	π	1	10	1	10	$\pi/2$	$3\pi/2$	0.001
HG2	0.1	$-\pi$	1	10	1	10	$-\pi/2$	$-3\pi/2$	0.001
HG3	0.1	π	1	10	1	10	$\pi/2$	$3\pi/2$	0.001
HG4	0.1	$-\pi$	1	10	1	10	$-\pi/2$	$-3\pi/2$	0.001

Each tower can be mounted on 2 different holes on the same belt as a first adjustment link. These holes have different distances from the belt center in the Sagittal axis. The hole should be chosen based on the subject's hip or torso span. The locations of the holes are provided in Table 1 with RH1 and RH2 indicating the right side. The second adjustment is a prismatic link in the transverse axis between Shaft 1 or Shaft 2 and Shaft 3. It should be adjusted to minimize the vertical distance of the human shoulder with the exoskeleton's elevation joint. Shafts 1 and 2 are usually used for short and tall subjects, respectively. These two adjustments (hole selection and prismatic vertical adjustment) are not considered as joints and should be fixed for simulation and usage. The prismatic adjustment between Shaft 1 or Shaft 2 and Shaft 3 is relevant to the vertical distance of the SJC with the LJC. According to the anthropometric data reported in the literature [82], the adjustment is calculated from Equation (6).

$$d = h\left[0.2289s + 0.2199\left(1 - s\right)\right] - l \tag{6}$$

where

d	the adjustment distance in meters of Shaft 1 or Shaft 2 with Shaft 3
h	the height of the subject in meters
s	the sex parameter (for a male is 1 and for a female is 0)
l	the exoskeleton maximum vertical distance for Shaft 1 (0.4820 m) and Shaft 2 (0.5570 m)

The joints are connected serially from Shaft 3 to the mechanism segments. The first 5 revolute joints in the vertical direction, like hinges (HG), connect 5 Slices and the Shaft 3 together like an accordion. The vertical direction of the sixth revolute joint connects the last Slice in HG5R and the Link. The last exoskeleton joint is the revolute joint in the direction of the shoulder elevation (E) that connects the Link to the mechanism. The last joint has a limited range of motion (ROM). The assistive torque of this elevation joint is applied with a passive mechanism or actuator (controlled motor).

The first 6 revolute joints are in the vertical direction (in the transverse plane) and are mainly responsible for keeping the exoskeleton's elevation joint at the desired location. The minimum number of required joints to provide this function is 3 revolute joints. These revolute joints can move the last joint (elevation joint) in the traverse and the frontal direction and pose as a desired orientation for the Link segment. If only 3 joints are used, the number of Slices is 3 (as opposed to 6), and they should be longer to cover the full horizontal SAA ROM. By increasing the number of these joints from 3 to 6 and increasing the number of Slice segments from 3 to 6, the dimension of these slices can be smaller. Using smaller slice segments helps in achieving a compact exoskeleton. However, increasing the number of the Slice segments and the connective joints leads to redundancy problems during simulation. Calculating the state of a redundant system requires extra calculation, relying on guessing the joint angles and depending on the initial joint angles.

The first 5 revolute joints in the EVO upper limb exoskeleton have a novel elastic rope that goes through holes on the slices. One end of the rope is connected to the last slice, and the other end is connected to the Shaft3. This elastic rope creates weak springs to keep the accordion-like system in its original location. In addition, the rope introduces a constraint to the 5 joints that inhibit the hinges from rotating in the undesired direction. The hinge's rotational springs and constraints are modeled using Equation (7) (symbolically shown in Figure 5a). Equation (7) was originally adopted from [83] to model the stiffness. The equation constrains the maximum range of rotation and is equipped with a rotational spring model of the elastic rope. The passive joint parameters of the hinge were assumed by the authors as listed in Table 2. These assumed parameters have no impact on the elevation mechanism and the assistive torque, which are the main focus of this research.

$$T_{Hinge} = -K\left(\varphi - \varphi_0\right) + k_1 e^{-k_2\left(\varphi - \varphi^-_{\max}\right)} - k_3 e^{k_4\left(\varphi - \varphi^+_{\max}\right)} - c\dot{\varphi} \tag{7}$$

where

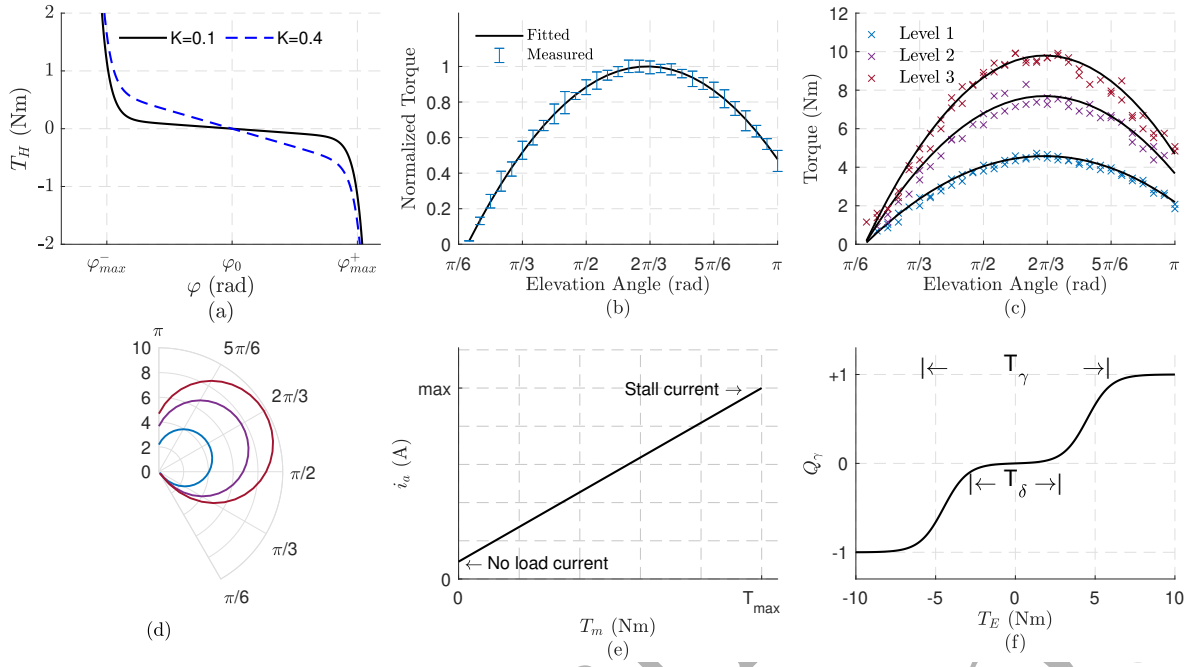

Fig. 5: (a) Plot of the first 5 revolute joints' passive torques with rotational spring (K) and maximum ROM (φ_{max}). (b) The normalized passive joint torque to the maximum of fitted data, (c) the measured passive joint torque for spring system levels 1 to 3, and (d) a polar indication of joint torque. All the measurements were done with zero rotational shift adjustment for (b-d). (e) The relation of the motor torque (T_m) and armature current (i_a) with motor torque constant (k_m). (f) The smooth curve of the human elevation torque using the dead zone torque (T_δ) and the threshold torque (T_γ).

T_{Hinge}	the passive torque of the hinge joints
K	the spring constant, in Nm/rad
φ	the joint angle in radian
φ_0	the unstretched angle of the rotational spring, in radian
k	the passive parameters of the constraint
$\varphi^-_{\max}$	the maximum ROM for negative direction
$\varphi^+_{\max}$	the maximum ROM for positive direction
c	the rotational linear damping coefficient
$\dot{\varphi}$	the joint's instantaneous angular velocity

3.2.3 Passive mechanism model

As mentioned in the introduction, the passive exoskeleton is primarily equipped with a spring mechanism that stores potential energy from human motion. The assistive joint torque profile varies based on the task [20]. The EVO upper limb exoskeleton can aid in positive elevation direction (flexion or vertical abduction) using a compressed spring and a cam mechanism (Figure 6a). In addition, it can have different spring strengths and minor rotational shift adjustments for the torque profile.

We have simultaneously measured the assistance force relevant to the elevation angle using a digital gram scale positioned perpendicular to the armrest and a digital inclinometer. The torque is computed by the measured force and length between the scale and the rotation axis. Finally, the joint torque was fitted with a 2-degree polynomial presented in Equation (8). The resultant torque-angle profile is shown in Figure 5b-d.

$$T_{Passive} = T_{max}\left[p_2\left(\varphi+\varphi_0\right)^2 + p_1\left(\varphi+\varphi_0\right) + p_0\right] \tag{8}$$

where

p_i	the polynomial coefficients ($p_2 = -0.4582$ 1/rad2, $p_1 = 1.9003$ 1/rad, and $p_0 = -0.9704$)
T_{max}	the maximum passive joint torque, which is 4.578, 7.693, 9.798 Nm for the Level 1, 2, 3 springs of EVO, respectively

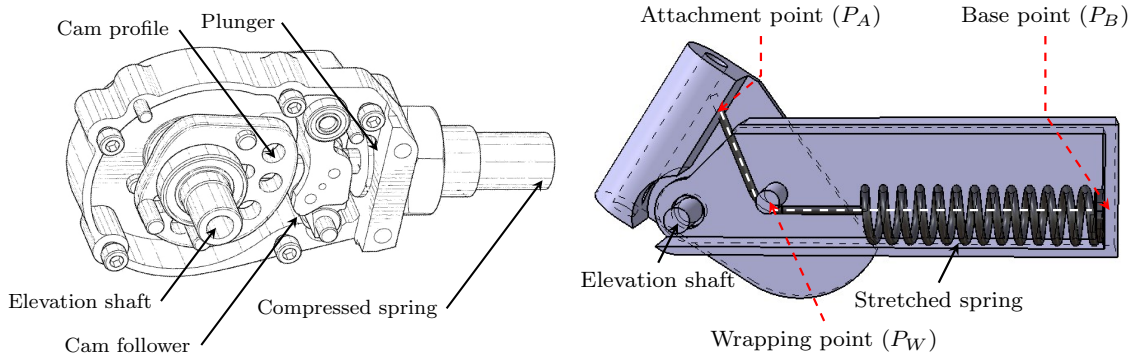

(a) EVO mechanism [84] (b) Custom mechanism

Fig. 6: Views of the passive elevation joint mechanisms assembled using a compressed spring (a) or stretched spring (b). (a) Evo providing an assistive torque to the upper arm of a wearer via a compressed spring [84]. (b) Our designed custom mechanism (adopted from Nasr et al. [20]) delivering passive torque via a stretched spring that wraps around a point P_B.

φ	the exoskeleton's elevation angle in radian
φ_0	the passive mechanism rotational shift (between -0.175 to 0.175 rad)

We created the custom mechanism depicted in Figure 6b (previously presented in [23]). The assistive passive torque of the mechanism (at the elevation shaft) is given by Equation (9). In Equation (9), $|\mathbf{P}_W - \mathbf{P}_B|$ and $|\mathbf{P}_A - \mathbf{P}_W|$ are the length from the base point to the wrapping point and the wrapping point to the attachment point, respectively. Thus, the spring deflection is the absolute value of the base-wrap-attachment path minus the initial spring length (L_0). In addition, the direction of the $\mathbf{P}_A - \mathbf{P}_W$ vector defines the direction of the spring tensile force to the attachment point. Finally, the consequent torque is defined as the cross-product of the position vector to the attachment point (from the rotation center) and the spring force. We assume the cylinder radius to be negligible; thus the wrapping point is the center of the cylinder in Figure 6b. The length of the spring decreases as the angle of the elevation joint increases. Simultaneously, as the angle of the joint increases, so does the moment arm of the spring force. As shown in the custom mechanism (Figure 6b), as the angle of the elevation joint increases, the moment arm increases while the spring length decreases. The delivered passive torque is produced by the combination of decreasing the force of the spring (due to shorter spring length) and increasing the moment arm of that force. Even though the spring is linear, the mechanism assembly is designed to produce a nonlinear torque-angle relationship (plotted in Figure 11a).

$$T_{Passive}(\varphi) = \left| \mathbf{P}_A \times k \left[\frac{\mathbf{P}_A - \mathbf{P}_W}{|\mathbf{P}_A - \mathbf{P}_W|} \left(|\mathbf{P}_A - \mathbf{P}_W| + |\mathbf{P}_W - \mathbf{P}_B| - L_0 \right) \right] \right| \tag{9}$$

where

k	the spring stiffness proportional constant
L_0	the initial length of the spring (equilibrium position)
$\mathbf{P}_A$	the coordinates of the attachment point relative to the frame at the elevation shaft
$\mathbf{P}_W$	the coordinates of the wrapping point relative to the frame at the elevation shaft
$\mathbf{P}_B$	the coordinates of the base point relative to the frame at the elevation shaft

3.2.4 Powered actuator model

Preliminary robotic exoskeletons and prostheses employed pneumatic and hydraulic actuators tethered to off-board bulky air compressors and fluid pumps resource stations, respectively [14, 85]. However, research and industry have moved to electromagnetic actuators, particularly brushless and brushed direct current motors [14, 85]. Motors are most efficient at high speeds and minimal torques, with rough torque densities of 15 Nm/kg and power densities of near 200 W/kg, and a 90% efficiency [86]. On the other hand, human muscle groups have torque and power densities of roughly 20 Nm/kg and 50 W/kg, respectively, with a concentric contraction efficiency of around 30% [86]. To increase the motor torque output to the robot's joints, electric motors are combined with a high-ratio transmission (mostly harmonic gearing); this design

Table 3: The electrotechnical specification of BLDC motor with or without a gearbox from CubeMars Co. (Nanchang, China).

#	Motor Model	Gear Ratio	Nominal Torque (Nm)	Rotor Inertia (kgm2)	Viscous Damping Coefficients (Nms/rad)	Motor Weight (kg)	Nominal Rotary Speed (rad/s)	Nominal Input Current (A)	Torque Constant (Nm/A)	Input Voltage (v)
1	AK80-64	64	48	564e-7	0.065	0.850	2.93	6.3	0.119	24-48
2	AK10-9 V2.0	9	18	1002e-7	0.130	0.960	23.67	11.8	0.16	24-48
3	AK10-9 V1.1	9	15	1002e-7	0.101	0.820	46.60	18.5	0.095	24-48
4	AK80-9	9	9	607e-7	0.054	0.485	25.66	12.0	0.091	24-48
5	AK80-6	6	6	607e-7	0.054	0.485	38.22	12.0	0.091	24-48
6	AK70-10	10	8.3	414e-7	0.034	0.521	41.89	8.8	0.095	24-48
7	AK60-6 V1.1	6	3	243e-7	0.021	0.368	23.04	4.5	0.113	24
8	R100 KV90	1	3.7	2505e-7	0.221	0.731	397.94	35.0	0.106	48
9	R80 KV110	1	1.3	758e-7	0.060	0.354	481.71	15.0	0.0868	48

allows for precision position control and causes the robotic actuator to have a high mechanical impedance (i.e., high inertia and mechanically stiff) [87]. However, utilizing actuators with high output impendence in wearable robots generally increases energy consumption and electric motor peak power requirements [87]. Thus, it is evident that designing a wearable robot actuator requires considering the primary actuator dynamic, which was ignored in designing active-passive exoskeletons to the best of our knowledge.

The following design requirements should be achieved to reduce system inefficiencies: low electric power consumption, low inertia and impedance, and high torque density motors with little gearing. To attain low mechanical impedance, high energy efficiency, and back-drivability, torque-dense motors with low ratio transmissions, also called direct-drive actuators, have been deployed in recent years [88]. Developments in high torque-density (torque per unit mass) BLDC motors by the drone industry have significantly fueled the use of low transmission ratios in wearable robots. The design of BLDC motors increases delivered torque by rising motor torque-density instead of the transmission ratio, decreasing the impacts of high gearing (i.e., backlash, torque-dependent Coulomb friction, increased weight, and the actuator's effective inertia and damping, which scale with the square of transmission ratio) [86, 87]. Thus, to overcome the resistance and back drive the actuator, significant external loads are required when the active component in an active-passive exoskeleton is off. The properties of high gearing systems introduce dynamic stiffness in physical interactions between humans and active machines. Recently, following the mentioned actuator design concepts, the MIT Cheetah legged robot was built using pancake-style BLDC motors with encapsulated windings [89].

The electromechanical characteristics of commercial BLDC motors were gathered in Table 3. The most critical motor specifications are effective inertia and nominal torque. In active-passive exoskeletons, when the actuator is turned off, and only the passive component is utilized, the actuator should have the lowest output inertia. Furthermore, the needed torque should always be smaller than the nominal torque. The achievable speed lowers as the required torque grows and the motor heats up.

A motor's torque-producing ability is usually expressed as Equation (10) and Figure 5e. Here, we are not considering an electrical equation such as the motor-armature inductance. The gear ratio (N) generates a rise in torque at the load and consequently a decrease in the load's speed. Without considering the loaded dynamic, the net output torque can be determined by considering the motor rotor inertias and the rotator viscous friction coefficients as seen in Equation (11) [90].

$$T_m = k_m i_a \tag{10}$$

$$T_{Output} = NT_m - \left(N^2 I_m \ddot{\varphi} + N^2 b_m \dot{\varphi}\right) \tag{11}$$

where

T_m	the torque applied to the rotor
k_m	the motor torque constant

Table 4: The coordinates location, mass, COM, and inertia matrix of the actuator cover.

Part Name	Parent Coordinate	Center of Mass (m)	Mass (kg)	Inertia Matrix (kgm2)					
				I_{xx}	I_{yy}	I_{zz}	I_{xy}	I_{xz}	I_{yz}
Motor	E	-0.042, 0.000, 0.000	0.669	75e-5	51e-5	50e-5	0	-1e-5	0
Housing	E	0.015, -0.050, 0.000	0.144	32e-5	17e-5	25e-5	4e-5	0	0
Arm	HG5	-0.005, 0.024, 0.061	0.069	4e-5	4e-5	1e-5	0	1e-6	0

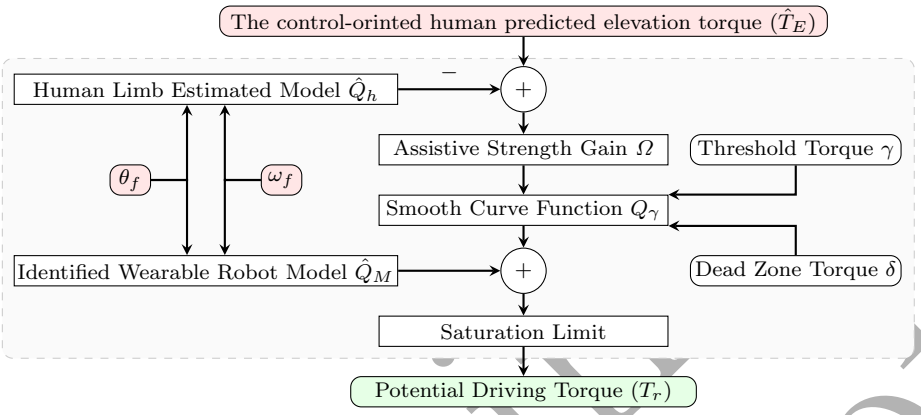

Fig. 7: Block diagram of the mid-level controller of the hierarchical AAN-computed-torque method (CTM) control architecture of active-passive exoskeleton robots. The mid-level controller defines the potential driving torque using the human and exoskeleton model [33].

i_a	the armature current
T_{Output}	the net output torque
N	the gear ratio
I_m	the motor rotor inertias
b_m	the rotator viscous friction coefficients

These pancake BLDC motors have average 10 cm diameter, 7 cm height, and 0.669 kg mass. The covering and fixture inertia properties are provided in Table 4 for an average motor dimension.

3.2.5 Hierarchical assistance model

High, mid, and low-level controllers are used in advanced hierarchical control of robotic exoskeletons, prosthesis, assistive, and rehabilitation systems [31, 33]. Primary, the high-level controller is in charge of understanding the user's motion intent for robotic prosthesis systems or the torque and force exerted by the user for wearable robotic systems [67, 68]. Here we assume that the human active torque ($\hat{\tau}_a$) is predicted accurately by the high-level controller. On the other hand, the low-level controller is in charge of directly commanding the robotic actuators considering the sensed robotic joint variable, following the desired torque (τ_d) that is generated by the mid-level controller [31, 33, 34]. Here, we assumed the low-level controller has a one-to-one model and can apply the desired torque (τ_d) accurately. Finally, the mid-level controller uses the high-level controller's determined intended motion or force/torque and defines the low-level controller's command [33]. The details of the mid-level controller is described in the following paragraph.

Recently, the AAN-CTM technique, which boosts rather than replaces motor activity, has shown encouraging outcomes for the mid-level controller [33]. Here, we adopted the controller in [33] (Equations (12-17)), considered the full AAN approach, and designed it to provide the required assistance torque (Figure 7). This unique approach finds the desired actuator torque by boosting the human active torque via the desired strength variable (Ω) and combining the robot's powered actuator model in Equation (15). The comprehensive model was presented using Equations (12, 13). The hyperbolic Equation (13) (symbolically shown in Figure 5f) eliminates the controller chattering effect in the presence of low human joint torque. In the simulation, the desired elevation torque (T_E) was calculated using the human shoulder joint torque and Equation (14). In practice, the elevation torque ($\hat{T}_E$) is estimated from the high-level controller using human data, for example, with MuscleNet [67, 68] and a wireless sEMG sensor, as shown in Figure 1. The maximum motor nominal torque limits the desired assistive output torque to mimic the practical actuation limit in Equation (16). The desired input current (i_a) calculated with Equation (17) should be driven by the hierarchical low-level actuator controller, which is primarily a servo controller.

$$T_d = \Omega Q_\gamma \hat{T}_E + \hat{Q}_M \tag{12}$$

$$Q_\gamma = \left| \frac{1}{1+e^{-\frac{4}{T_\gamma - T_\delta}\left(\hat{T}_E - \frac{T_\gamma + T_\delta}{2}\right)}} - \frac{1}{1+e^{\frac{4}{T_\gamma - T_\delta}\left(\hat{T}_E + \frac{T_\gamma + T_\delta}{2}\right)}} \right| \tag{13}$$

$$T_E = \left({}^{G}R_{UA} \begin{bmatrix} \tau_{SAA} \\ \tau_{SMLR} \\ \tau_{SFE} \end{bmatrix} \right) \bullet \left({}^{G}R_{E} \begin{bmatrix} 1 \\ 0 \\ 0 \end{bmatrix} \right) \tag{14}$$

$$\hat{Q}_M = N^2 \hat{I}_m \ddot{\varphi}_f + N^2 \hat{b}_m \dot{\varphi}_f \tag{15}$$

$$T_r = min\left(max\left(T_d, -NT_{max}\right), NT_{max}\right) \tag{16}$$

$$i_a = \frac{1}{N\hat{k}_m} T_r \tag{17}$$

where

T_d	the desire assistive output torque
Ω	the robot's desired assistive strength variable, which is positive for assistive and negative for resistive (rehabilitation) control
$\hat{T}_E$	the human predicted elevation torque by the high-level controller
Q_γ	the smooth curve of the human elevation torque between the dead zone and the threshold torque
$\hat{Q}_M$	the identified wearable robot actuator model, the result of the rotor inertia and the viscous damping
T_γ	the positive threshold torque
T_δ	the positive dead zone torque
${}^{G}R_{UA}$	the rotation matrix of the upper arm frame relevant to the global reference frame
${}^{G}R_{E}$	the rotation matrix of the mechanism frame attached to the elevation joint relevant to the global reference frame
τ_{SAA}	the human SAA joint torque
τ_{SFE}	the human SFE joint torque
τ_{SMLR}	the human SMLR joint torque
$\dot{\varphi}_f$	the actuator joint angular velocity that is calculated with the derivative of the joint angle
$\ddot{\varphi}_f$	the actuator joint angular acceleration that is calculated with the derivative of the joint angular velocity
T_r	the potential driving torque, which is saturated by the maximum motor torque
T_{max}	the maximum nominal motor torque
$\hat{k}_m$	the identified torque constant

3.3 Closed-kinematic system

Here, the connection of the exoskeleton to the human, the combined model, and the requirements of simulation are described.

3.3.1 Exoskeleton-human interaction

The belt of the exoskeleton fastens around the hip or connects to the LJC. The LJC is estimated as 26.4%, 0% and 12.6% (for male) of the Pelvis width on the X-, Y- and Z-axes, or 28.9%, 0% and 17.2% (for female), respectively. The Z-axis is in the direction of the left-to-right anterior superior iliac spine (the most prominent point on the anterior superior spine of the right and left ilium). The X-Z plane is formed with the Z-axis and the midpoint between the postero-superior iliac spines (the prominent points on the right and the left ilium's posterior superior spine). In total, the assistive torque reaction on the shoulder conveys to the exoskeleton belt and, consequently, to the hip. The belt of the exoskeleton and the LJC of the human are rigidly connected. For future studies, the connection can be modeled with a spring and damper [91].

The exoskeleton's armrest is attached to the human upper arm with a specific joint. The specific joint is a 1-DoF revolute joint, which allows for one rotational DoF about the common axis. The common axis is the Y-direction of the upper arm (the line connecting the elbow joint center (EJC) to the SJC, pointing proximally). The connected 1-DoF revolute joint can easily rotate around the Y-axis, but has 5 constraints

that prevent rotation in the X- and Z-direction and translation in all directions of the human upper arm coordinate system. The mentioned 5 constraints convey the interaction forces and torques to the human upper arm from the exoskeleton's armrest. The interaction forces and torques result from the configuration of the human-exoskeleton connections and the assistance torque by the passive mechanism and powered actuator.

3.3.2 Multibody model

The stated two connections at the exoskeleton's belt and armrest to the human hip and upper arm form the closed kinematic loop. The closed kinematic loop and the joint system configuration cause some exoskeleton joints to be kinematically dependent on the human joints [20]. Since the generalized coordinates (q) and generalized speeds (p) are dependent, the multibody system dynamic equations can be derived with the constraint reactions occurring explicitly in Equation (18), which are DAEs model.

$$\mathbf{M}_{n\times n}\dot{\mathbf{p}}_{n\times 1} + \mathbf{C}_{n\times m}\boldsymbol{\lambda}_{m\times 1} = \mathbf{F}_{n\times 1} + \mathbf{Q}_{n\times 1} \tag{18}$$

$$\Phi(\mathbf{q}_{n\times 1}, t) = 0 \tag{19}$$

$$\Psi(\mathbf{p}_{n\times 1}, \mathbf{q}_{n\times 1}, t) = 0 \tag{20}$$

$$\chi(\dot{\mathbf{p}}_{n\times 1}, \mathbf{p}_{n\times 1}, \mathbf{q}_{n\times 1}, t) = 0 \tag{21}$$

where

$\mathbf{M}$	Mass matrix, a combination of the human model, the exoskeleton, and the mass matrixes of the assistive components
$\mathbf{C}$	Coefficient matrix of constraint reactions
$\boldsymbol{\lambda}$	Reaction forces and torques in the cotree joints that enforce the kinematic constraint of human-exoskeletons connection
$\mathbf{F}$	The right-hand side of dynamic equations
$\mathbf{Q}$	The vector containing the applied wrench (torque/force) at the joints, which consists of the human joint torque (τ) and the robot joint torque (T)
Φ	Position-level kinematic constraint equations
Ψ	Velocity-level kinematic constraint equations; if the generalized speeds are equal to the coordinate derivatives, then $\Psi = \dot{\Phi}$
χ	Acceleration-level kinematic constraint equations
$\mathbf{q}$	Generalized coordinates of the multibody system, which consists of the human joint angles (θ) and the robot joint states (φ)
$\mathbf{p}$	Generalized speeds of the multibody system, which consists of the human joint angular velocities (ω) and the derivative of robot joint states ($\dot{\varphi}$)
n	number of joints
m	number of constraint reactions

3.3.3 Multibody analysis

The human-exoskeleton closed-loop system has 10 algebraic constraints (5 for each side). These 5 constraints are due to the human-exoskeleton interaction forces and torques described in section 3.3.1. The human body model itself has 20-DoF (section 3.1.1). The exoskeleton should have at least 10-DoF (5-DoF for each side) to avoid decreasing, resisting, or locking the human DoF. In total, the multibody system was modeled using 30 generalized coordinates coupled with 10 algebraic constraints. Specifically, there are 20 human joint angles (θ), 10 robot joint states (φ), and 10 reaction forces and torques (λ).

3.3.4 Simulation requirement

The human upper limb with the shoulder exoskeleton forms a closed-kinematic loop. In contrast to an open-kinematic chain, a combined exoskeleton produces residual forces/torques if the exoskeleton DoF are inadequate to align with the motion axis of a human joint, or if there are any human-robot kinematic differences [92, 93]. A limited number of passive or self-adjusting joints are utilized to address this issue [94]. For example, the mentioned EVO exoskeleton has utilized 6 passive joint configurations (section 3.2.2).

Theoretically, the human joint angles are determined by the measured human joint trajectory (section 2) or the CNS (section 3.1.2). The exoskeleton joints angle, angular velocity, and angular acceleration should

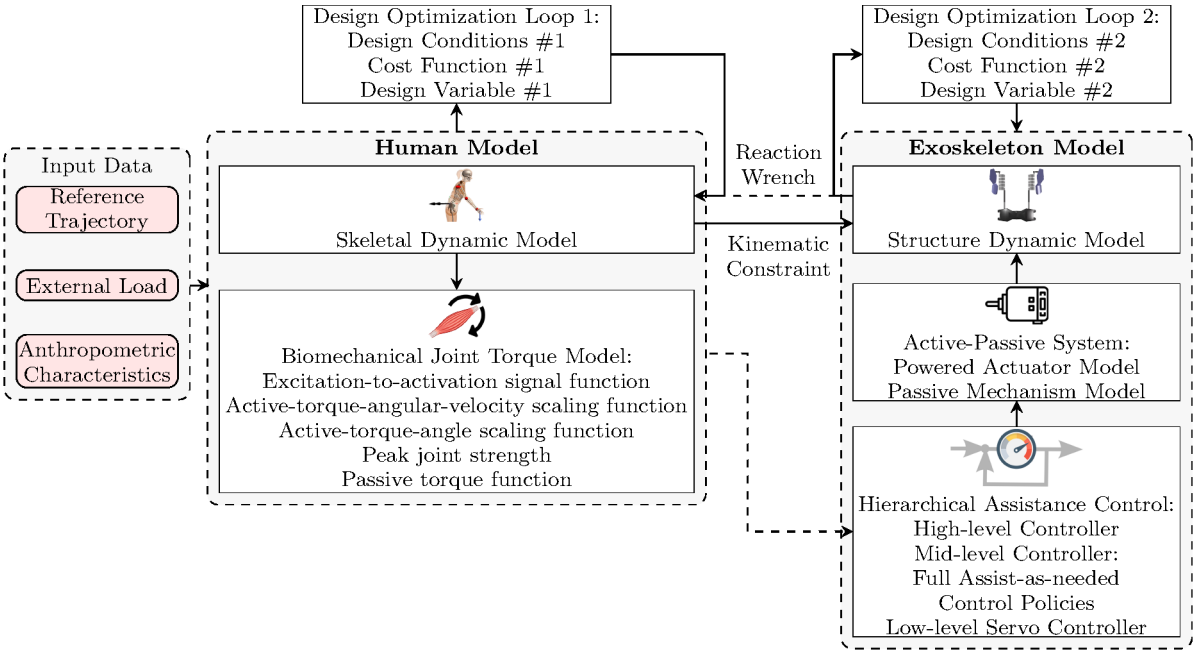

Fig. 8: Schematic of designing, synthesizing, analyzing, and optimizing the inverse scenario.

be defined by the human kinematic using Equations (19-21). The initial conditions of the exoskeleton joints are ignored or guessed by the software at the start of the simulation.

Simulating the redundant configuration introduces hardships when calculating the initial joint angles in simulation software like MapleSim. Calculating the initial joint angles has no unique solution and has infinite solutions. One solution is to apply a virtual prismatic joint with liner springs parallel to the system of the second and fifth revolute Hinges joints (shown in Figure 3b). Using the virtual prismatic joint increases the chance of choosing a realistic solution from infinite options.

As mentioned in section 3.2.2, there are 6 joints in the Y-direction. When the five Slices are aligned or fully extended, the closed kinematic chain experiences a singularity, introducing an impulsive force internally. Particularly, the required torques to move from that specific configuration are infinite. Using the mentioned elastic rope in practice or using the hyperbolic function of Equation (7) in simulation, introduce a constraint. The constraint inhibits the singularity configuration from happening.

4 Design optimization

4.1 Overall method

The exoskeleton actuator designing process is achieved through forward or inverse simulation of the multi-body dynamic system (depicted in Figure 8 and Figure 9). So far, the inverse scenario (section 4.1.1) was used to find the passive mechanism's optimum design [20], which is not controlled by the system and is a function of joint angle, not time. The forward scenario (section 4.1.2) is used to evaluate the optimum actuator parameters for motor control, which depends on the human intention prediction. Broadly, the active component is controlled as a function of time. The desired motion trajectory (generalized coordinates, speeds, and acceleration), the human, and the exoskeleton information are necessary for both scenarios.

4.1.1 Inverse scenario

The inverse scenario benefits from computationally efficient simulation [20]. However, in the inverse simulation, the impact of the human actuation torque is ignored in the active exoskeleton control. The inverse scenario is similar to forward simulation when high assistance strength is selected. As shown in Figure 8, initial optimization is done with the reaction wrench variable having minimal human activation torque. This first optimization loop is constructed from the human dynamic system without an actuator dynamic model to guess the optimum assistive exoskeleton torque. The second optimization loop is constructed to design the actuator parameter. The second loop produces the output torque similar to the optimum assistive torque from the first optimization loop.

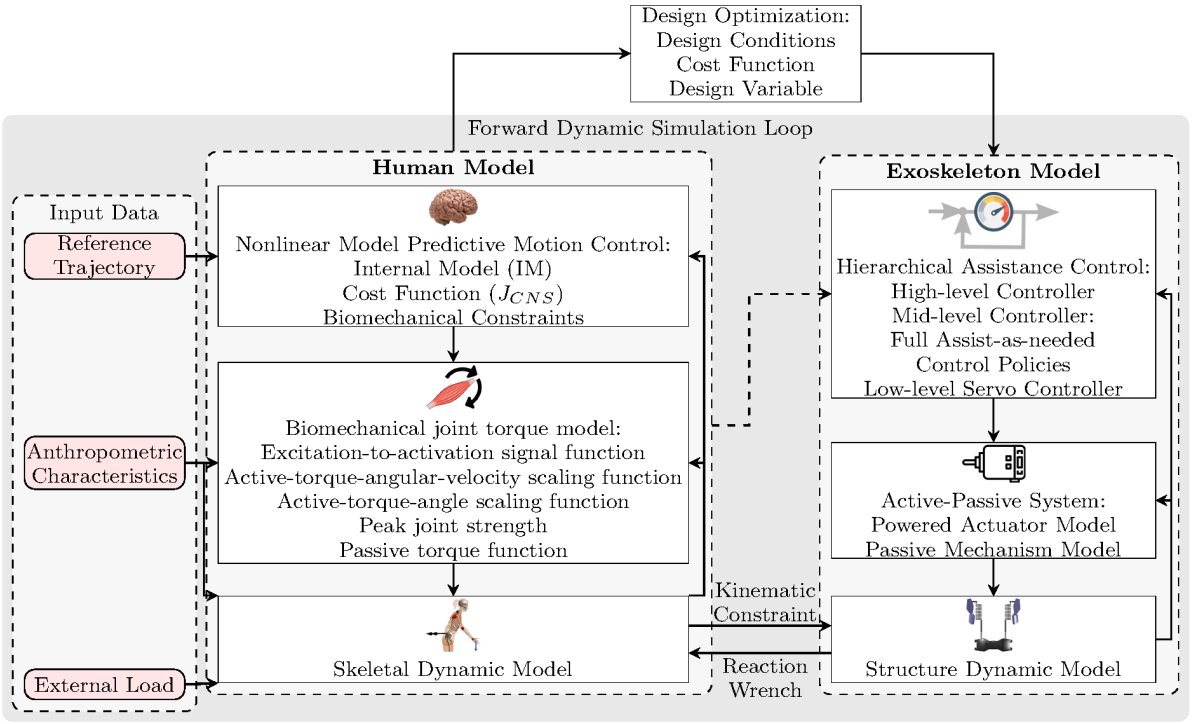

Fig. 9: Schematic of designing, synthesizing, analyzing, and optimizing the forward scenario.

Here, the inverse scenario was used to design the custom passive mechanism. Precisely, the first loop optimized the passive torque-angle profile and the second loop optimized the mechanism parameters outlined in Equation (9).

4.1.2 Forward scenario

The forward scenario benefits from a comprehensive and similar simulation to the human-robot interaction. However, the forward simulation is time-consuming. As shown in Figure 9, the primary step is designing, synthesizing, analyzing, and optimizing the actuator model via the optimal controller, which acts as the CNS and contributes to the forward dynamic simulation of the human-robot model. The procedure starts with an optimal controller that follows the desired trajectory and commands the human (excitation or activation) signal or (active or joint) torque. Both the actuator command (defined by the assistance model [33]) and human input are injected to the forward dynamic simulation of the multibody system. The optimization loop evaluates the objective function and finally guesses and selects the actuator parameter.

4.2 Design variables

A design variable is a numerical input that can be changed during design optimization. Optimization of the actuator can be achieved by changing the properties of the passive mechanism and selecting the BLDC motor.

As mentioned in section 3.2.2 and modeled in Equation (8), there are two variables in the passive mechanism. First, the maximum passive joint torque (T_{max}), which is 4.578, 7.693, 9.798 Nm for the Level 1, 2, 3 springs of EVO, respectively. The second variable is the passive mechanism rotational shift (φ), which can be adjusted between -0.175 and 0.175 rad.

The addition of an actuator, although it introduces additional inertia (Table 4) and viscous rotator friction to the system, can provide active torque with the required actuator control system. The active torque is modeled in Equation (11), and the maximum possible nominal torque is provided in Table 3 for 9 motors. The optimization design variable is the selection of the BLDC motor from Table 3.

Table 5: The details of 5 conditions of human and exoskeleton systems optimization.

Symbol	Condition	Human	Exoskeleton	Design Variable				
			Inactive	Passive	Active	T_{max}	φ_0	Motor
H	only human	✓						
IE	human with inactive exoskeletons	✓	✓					
FP	human with fully passive exoskeletons	✓		✓		✓	✓	
FA	human with fully active exoskeletons	✓	✓		✓			✓
AP	human with active-passive exoskeletons	✓		✓	✓	✓	✓	✓

4.3 Design cost function

Industrial wearable exoskeletons are designed to assist and improve human performance to reduce user effort, fatigue, and, therefore, the risk of work-related MSDs [7, 9, 11, 12]. The performance metric that aims to minimize the cost function is one or a combination of the following variables.

The first variable is the human joint applied torque (Q) in Equation (1), which is the net torque applied to the skeletal system. This variable shows the required torque for the human motion without considering the active and passive components of the MTGs [78] in Equation (2).

The second variable is the human active torque (τ_a) in Equation (2) that only consider the passive torque that occurs when the muscles, tendons, and ligaments near the joints are strained [95]. In the MapleSim Biomechanics model, the human active torque is relevant to the active tension of the muscle.

The third variable is the human joint power. Theoretically, the quantity of energy converted in one unit of time is called power. In rotational joints, power is the product of the joint active torque (τ_a) and the angular velocity (ω).

The fourth variable is the muscles metabolic energy expenditure (MMEE). We have used the MMEE model [96] as a critical performance measure of human motion with or without wearing of the exoskeletons. The MMEE model is a general joint-space numerical model of metabolic energy expenditure obtained by combining the laws of thermodynamics and multibody system dynamics principles [96]. The equations of the energy model for zero co-contraction MTGs are as follows:

$$E = \int_0^{t_{max}} \left[\dot{h}_i + p_i\right] dt \tag{22}$$

$$\mathbf{p} = \boldsymbol{\tau_a}\boldsymbol{\omega} \tag{23}$$

$$\dot{\mathbf{h}} = \dot{h}_M \left|\boldsymbol{\omega}\right|_{(max)} \left|\boldsymbol{\tau_a}\right| + \dot{h}_{SL} \left|\boldsymbol{\tau_a}\boldsymbol{\omega}\right| \tag{24}$$

where

p	the mechanical power at the joint
$\dot{h}$	the heat rate
$\dot{h}_M$	the dimensionless heat rate for activation and maintenance, determined to be 0.054
$\dot{h}_{SL}$	the dimensionless shortening lengthening heat rate, 0.283 for positive power, and 1.423 for negative power
$\boldsymbol{\omega}_{(max)}$	the maximum angular velocity over the entire motion

In addition to the human-based design cost function, the electricity consumption of the actuator should be as low as possible. Precisely, the exoskeleton should provide the maximum portion of assistance using the passive mechanism. The actuator should have the role of adjustment or providing extra assistance whenever needed. Consequently, the electrical consumption of the actuator should be one element of the design cost function.

4.4 Design conditions

For a fair comparison, five conditions were considered to study the effect of exoskeletons on the human body. The exoskeleton can be inactive (provide no active and passive torque), and the human should be able to carry its mass around. The EVO exoskeleton's novel passive mechanism can be activated with a tiny leveler. The five conditions in Table 5 are constructed by combining the sub-models in section 3.

5 Results and discussion

The optimization checks the 966 possible simulations (6 Tasks (section 2.1), 5 conditions (section 4.4), 3 maximum passive torques, 5 passive mechanism rotational shifts (section 3.2.3), and 9 motors (section 3.2.4)), and the optimum results are presented in the following.

5.1 Human performance analysis

According to the simulation results, only the shoulders (SFE and SAA) and the torso (TFE, TRLLF, and TRLAR) variables change in the conditions mentioned in section 4.4. This result is compatible with the fact that the shoulder exoskeleton directly provides an assistive torque for the shoulder joint and indirectly increases the torque of the torso joint. Thus, here, Figure 10 provides the results of the design cost function in section 4.3 for the torso joints, the right, and the left shoulder.

The average of absolute active torque of the right shoulder joint (summation of SFE and SAA) for 5 conditions and 2 groups of tasks are shown in Figure 10a. When the exoskeleton is inactive, the average absolute active torque increases by approximately 1 Nm compared to not wearing the exoskeleton. This is due to the inactive exoskeleton weighing 3.461 kg, which the user should carry. By employing a passive exoskeleton with $T_{max} = 9.798$ Nm and $\varphi_0 = -0.175$ rad, the average of absolute active torque of the shoulder joint decreased by 13% and 53% for heavy object handling and arm reaching tasks, respectively. Using motor #3 and motor #1 for arm reaching and heavy object handling tasks reduced the average of absolute active torque by 79% and 49%, respectively. Using $T_{max} = 9.798$ Nm, $\varphi_0 = -0.175$ rad, and motor #4 for arm reaching task as well as $T_{max} = 9.798$ Nm, $\varphi_0 = -0.175$ rad, and motor #1 for heavy object handling task, the average of absolute active torque drops by 80% and 57%, respectively.

According to Figure 10b, the left shoulder has the same trend as the right side. However, the average of absolute active torque amount is lower than the right shoulder (Figure 10a) since the left arm has not contributed to lifting a heavy object in the overhead work task.

The average absolute active torque for the torso joint (Figure 10c) has not changed considerably. Using an inactive exoskeleton can decrease the average absolute active torque since it adds weight to the subject's back and helps in torso extension. If the subject bends with a larger angle, the exoskeleton's added weight would increase the required torque for torso extension. Since in a fully active and active-passive exoskeleton, the motor, housing, and shaft are added to the system near the elevation mechanism of the exoskeleton, the torso's torque increased by 1%.

The reaction force and torque at the attachments of the exoskeleton to the human (belt, right, and left armrest) are shown in Figure 10d to Figure 10i. According to these results, the reaction increases by providing a more assistive torque profile at the exoskeleton's elevation joint. This value should be considered for study to improve human comfort.

According to Figure 10j, the fully active and active-passive exoskeleton can lead to a metabolic energy expenditure drop. The metabolic energy expenditure decreases more for free motion and less for heavy object manipulation. One of the reasons behind this is that the motors are weak or limited by the maximum motor torque as seen in Equation (16). The other reason is that the active assistance augments power with the strength variable according to Equation (12).

5.2 Motor selection

According to the optimization results, three motors from Table 3 are the design candidates. Motor #1, which can provide the highest torque of 48 Nm, is suitable for heavy object handling assistance with or without the passive mechanism. The drawback of motor #1 is the high gear ratio and rotator inertia, which is not suitable for back-driving the motor while the motor is off.

Motor #3 is another suitable actuator that provides the highest assistance for the arm reaching task without adding as much back-driving difficulty as motor #1. In the case of a passive mechanism within the active component, motor #3 can be replaced with motor #4, which has lower rotator inertia but has the same gear ratio. The other positive point of motor #4 over motor #3 is its lighter body which is included in the modeling, simulation, and optimization section. The motor weight can be lighter when a passive mechanism is incorporated since a portion of the assistance torque is provided by the passive mechanism. It is unnecessary to use a heavy motor with the highest amount of torque.

As shown in Figure 1, the BLDC motor should connect to the computer using an adaptor. For safety, an emergency shut down switch may be handed to the user and should be located between the motor and power supply.

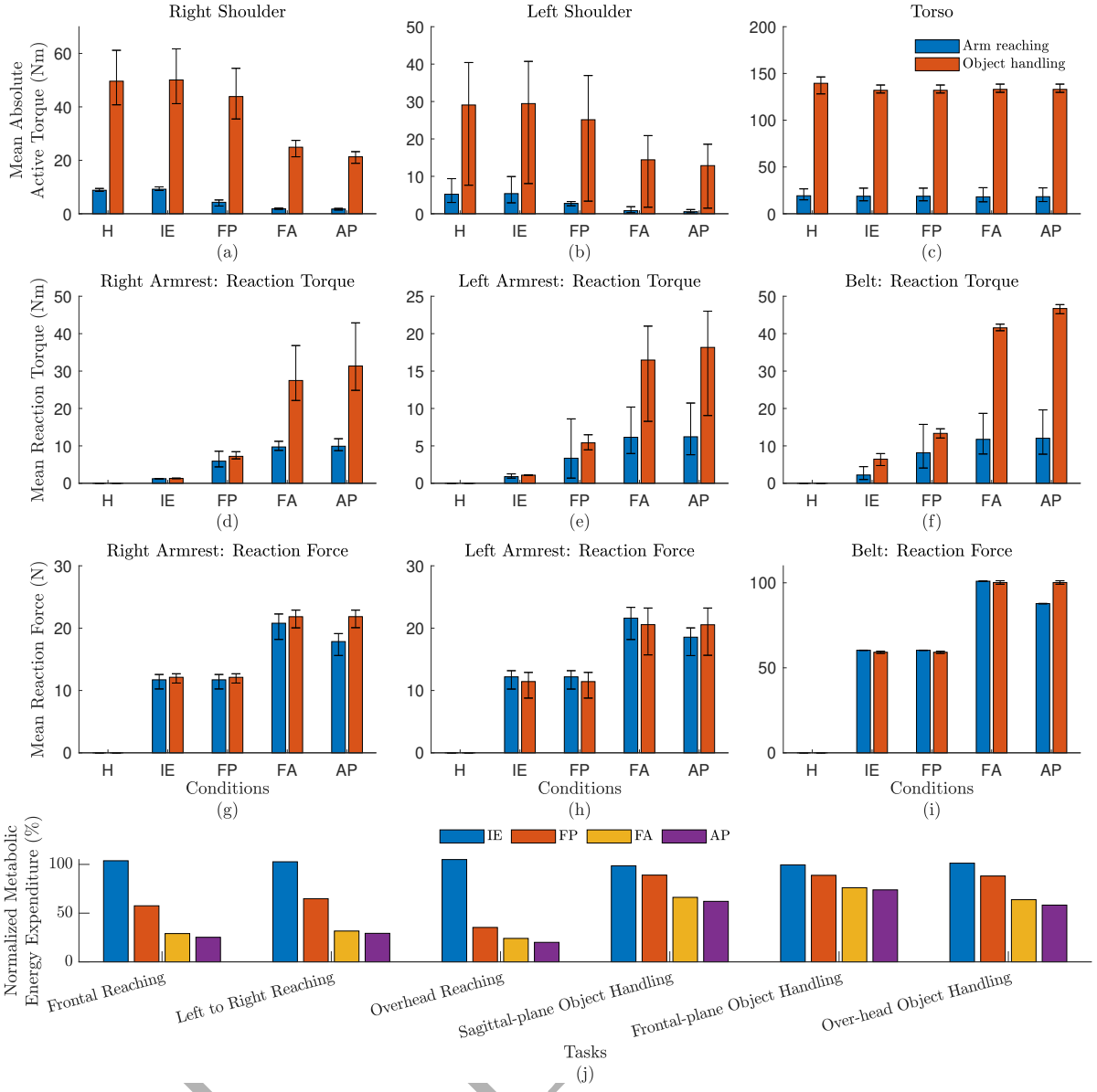

Fig. 10: The average of absolute active torque for the right shoulder, left shoulder, and the torso (a-c). The reaction torque and the reaction force at the right armrest, left armrest, and the belt (d-i). The metabolic energy expenditure of the human wearing the exoskeleton is normalized by the human not wearing the exoskeleton for 6 tasks (j). H: human, IE: inactive exoskeleton, FP: fully-passive exoskeleton, FA: fully-active exoskeleton, AP: active-passive exoskeleton.

5.3 Exoskeleton actuation comparison

According to the optimization outcomes, the order of the highest to lowest assistance is provided by the following systems: active-passive, fully active, fully passive, and inactive exoskeletons. The fully active can provide the same assistance as the active-passive exoskeleton if a stronger motor was available, but it would reduce the back drivability of the wearable robots. Sometimes, a stronger motor is unavailable with the desired back drivability, and consequently, the wearable robot is weaker than expected, requiring additional assistance. This fact leads to the user requiring crutches with a lower-limb exoskeleton or a technician group carrying the lower-limb exoskeleton worn by the patient [51].

The active-passive exoskeleton has advantages over a fully active exoskeleton from a weight perspective. The passive mechanism is 0.850 kg (Table 1) and can provide 9.798 Nm (section 3.2.3). Its torque-weight ratio (TWR) is, therefore, 11.52 Nm/kg. At the same time, motor #3 can provide 15 Nm when its weight is only 0.820 kg and requires, for example, a 2.4 kg battery to operate as used in the Technaid Exo-H3 exoskeleton. Consequently, motor #3 has a 4.65 Nm/kg battery TWR. Note that as the TWR increases, the

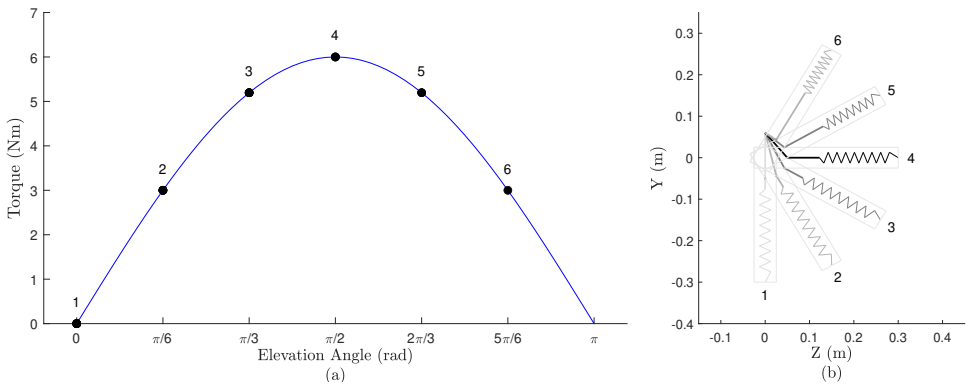

Fig. 11: (a) The custom passive mechanism torque-angle profile for the stretched arm motion designed by the first loop of the inverse scenario. (b) The depiction of the custom mechanism posture changes (without the attachment link). The 1-6 postures in (b) are marked with relevant generated passive torque in (a).

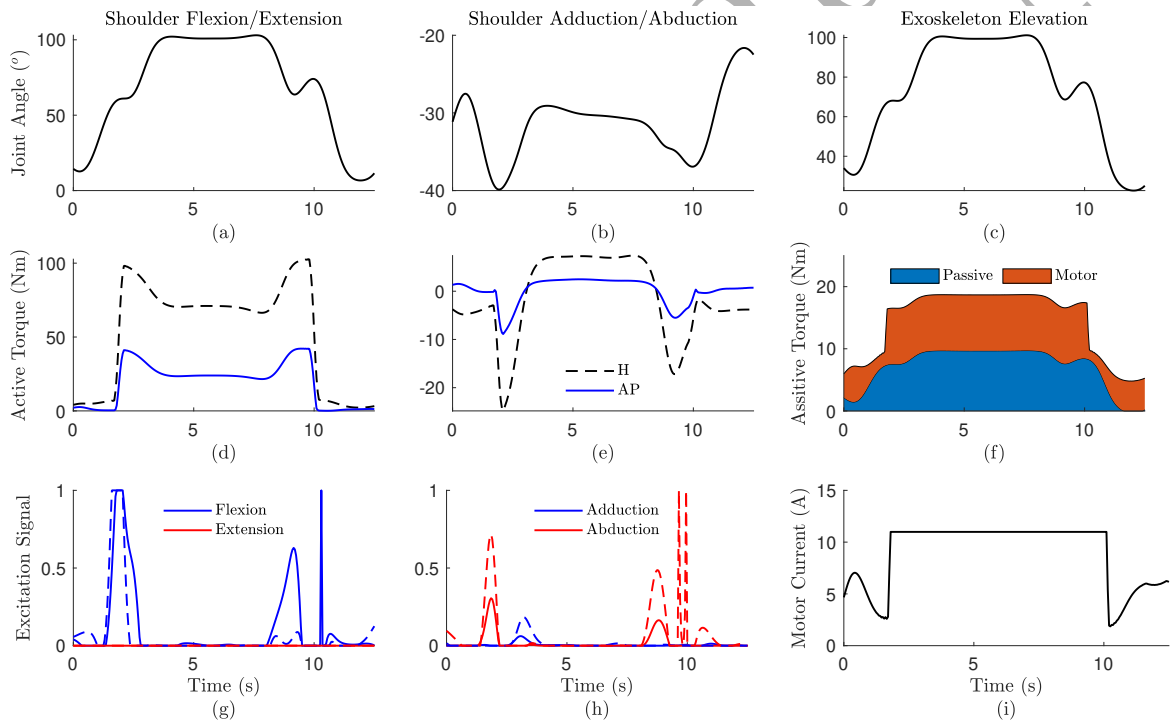

Fig. 12: The joint angle changes of the right SFE, SAA, and the exoskeleton's elevation (a-c). The activation torque of the right shoulder for the human-only condition (dashed) and the active-passive exoskeleton condition (solid) (d and e). The exoskeleton assistive torque of the passive mechanism and motor #4 (f). The excitation signal of the mentioned joint (g and h). The motor consumption current versus time is shown at (i).

portability and user comfort improves proportionally. Thus using the passive mechanism has advantages over the actuator, but it is impossible to provide the torque profile required as a function of time within the passive mechanism [12, 20]. Using active and passive assistance is prescribed in this condition as it benefits from a higher TWR of passive mechanism and flexible torque profile of actuator. This conclusion is similar to the literature results, which describe the contribution of the passive mechanisms to lowering the size, weight, and required active torque, advancing the portability [11, 18, 43].

From an energy consumption viewpoint, a weaker motor lowers the energy required to drive motors in Table 3. Using the passive mechanism along with the motor in the active-passive exoskeleton helps reduce the required electrical energy. The lower required electrical energy leads to a more lightweight energy storage unit (battery) in the portable exoskeleton [16, 97]. Alternatively, using the same battery, the working duration of the active-passive exoskeleton would be higher than the fully active exoskeleton.

To recap, the AAN control requires minimal motion from the human to estimate the contributed torque and the exoskeleton strengthens the human motion. Moreover, when the human motion is small, and the contributed torque is low according to the AAN, the exoskeleton's motor should not activate and should not restrict the motion (i.e. low stiffness). In other words, there should be a direct drive with small inertia and stiffness, without a large gear ratio. When the gear ratio is low, the produced torque from electrical motors is low. Thus, the fully active exoskeleton can produce limited torque because of the direct drive. However, the added passive mechanism has no inertia and stiffness that resists human motion, while providing torque in addition to the motor. Thus, the torque provided by passive mechanism works in harmony with the active motor torque.

5.4 Custom passive mechanism

The passive torque-angle profile for a general stretched arm motion (without heavy object manipulation) is shown in Figure 11a. To design this profile, the first loop of the inverse scenario (section 4.1.1) was used. For the mentioned assistive torque-angle profile, specific passive mechanism variables (Equation (10)) are necessary. Using the second loop of the inverse scenario (section 4.1.1), the spring stiffness proportional constant (k) was determined to be 2000 N/m and the initial length of the spring (L_0) was 0.25 m. The distance between the wrapping point and base point ($|\mathbf{P}_W - \mathbf{P}_B|$) was 0.25 m. The attachment point is located from the elevation joint at the π rad direction of the gravity (vertical line). When the elevation angle is 0, the distance between attachment point and wrapping point ($|\mathbf{P}_A - \mathbf{P}_W|$) was 0.06 m. The passive elevation joint mechanism at different angles are shown in Figure 11b.

5.5 Simulation example

As an example, a 10-second movement of an overhead heavy object (100 N weight) manipulation task was used with and without the active-passive exoskeleton condition, and the result is shown in Figure 12. The joint angle of the right SFE and SAA as well as the exoskeleton elevation, are shown in Figure 12a-c. The relevant active torque decreased by using the exoskeleton according to Figure 12d-e. As shown in Figure 12f, the passive torque of the exoskeleton is a function of joint angle [20], and the active or motor torque is a function of time. The motor torque provides extra assistance whenever needed, which was expected [20]. The excitation signal for positive and negative directions of the MTGs are shown in Figure 12g-h. The level of the excitation signal decreases when using the exoskeleton, i.e. less effort is required from the user. The motor's current is displayed in Figure 12i, which indicates that the motor is not overloaded according to the data on motor #4 in Table 3.

6 Conclusion

This research proposes a dynamic synthesis of passive and active assistive shoulder exoskeletons by incorporating a model with six components: the MapleSim Biomechanics upper-body dynamic model, an optimal controller, the exoskeleton rigid body, a passive mechanism, a powered actuator, and an assistance model. The six practical tasks for human motion used were frontal reaching, left to right reaching, overhead reaching, sagittal-plane object handling, frontal-plane object handling, and over-head object handling. The design optimization aimed to reduce the human-based and the exoskeleton-based criteria. According to the results, the active-passive exoskeleton provided more assistance to the human than the fully active and fully passive exoskeleton, while the weight of the exoskeleton did increase compared to the fully active exoskeleton. Additionally, the optimization offered a back-drivable motor with lower inertia, gear ratio, and viscous damping coefficients instead of a powerful motor that is not back-drivable. The active-passive exoskeleton would consume less electricity than the fully active exoskeleton, which helps design a lighter portable exoskeleton. In total, the optimized active-passive exoskeletons create lighter and smaller exoskeletons that lessen the user's muscular activation torque for the tasks being studied.

We expect future wearable exoskeletons to adopt components that incorporate passive and active assistance systems. Future studies should focus on the control design and propose a practical algorithm to control such a complicated but efficient actuation system as mentioned by relevant studies [33]. In addition, researchers may focus on energy harvesting by using the active motor to utilize positive power [97]. The last point to consider is safety and human comfort, which should be thoroughly examined before producing a commercial wearable exoskeleton.

Glossary

AAN assist-as-needed.
BLDC brushless direct current.
CNS central nervous system.
COM center of mass.
CTM computed-torque method.
DAE differential algebraic equation.
DoF degree of freedom.
EFE elbow flexion/extension.
EJC elbow joint center.
FPS forearm pronation/supination.
IM internal model.
IMU inertial measurement unit.
LJC lumbar joint center.
MMEE muscles metabolic energy expenditure.
MSD musculoskeletal disease.
MSK musculoskeletal.
MTG muscle torque generator.
NFE neck flexion/extension.
NMPC nonlinear model predictive control.
NRLAR neck right/left axial rotation.
NRLLF neck right/left lateral flexion.
ODE ordinary differential equation.
PWR power-to-weight ratio.
ROM range of motion.
SAA shoulder adduction/abduction.
sEMG surface electromyography.
SFE shoulder flexion/extension.
SJC shoulder joint centre.
SMLR shoulder medial/lateral rotation.
TFE torso flexion/extension.
TRLAR torso right/left axial rotation.
TRLLF torso right/left lateral flexion.
TWR torque-weight ratio.
WFE wrist flexion/extension.
WRUD wrist radial/ulnar deviation.

Acknowledgements This research is supported by funding from the Canada Research Chairs Program and the Natural Sciences and Engineering Research Council of Canada. The authors wish to thank Ekso Bionics Holdings Inc. for providing the Ekso EVO passive shoulder exoskeleton.

References

1. Fischer SL, Koltun S, Lee J (2021) A cross-sectional survey of musculoskeletal disorder hazard exposures and self-reported discomfort among on-shore wind turbine service technicians. Ergonomics 64(3):383–395, DOI 10.1080/00140139.2020.1831079
2. Khansa I, Khansa L, Westvik TS, Ahmad J, Lista F, Janis JE (2018) Reply: Work-related musculoskeletal injuries in plastic surgeons in the United States, Canada, and Norway. Plastic and Reconstructive Surgery 141(1):165e–175e, DOI 10.1097/PRS.0000000000004956
3. Nazari G, MacDermid J, Cramm H (2020) Prevalence of musculoskeletal disorders among Canadian firefighters: A systematic review and meta-analysis. Journal of Military, Veteran and Family Health 6(1):83–97, DOI 10.3138/jmvfh-2019-0024
4. Van Rijn RM, Huisstede BM, Koes BW, Burdorf A (2010) Associations between work-related factors and specific disorders of the shoulder - A systematic review of the literature. Scandinavian Journal of Work, Environment and Health 36(3):189–201, DOI 10.5271/sjweh.2895
5. Schopflocher D, Taenzer P, Jovey R (2011) The prevalence of chronic pain in Canada. Pain Research and Management 16(6):445–450, DOI 10.1155/2011/876306
6. Linaker CH, Walker-Bone K (2015) Shoulder disorders and occupation. Best Practice and Research: Clinical Rheumatology 29(3):405–423, DOI 10.1016/j.berh.2015.04.001
7. Zhou X, Zheng L (2021) Model-based comparison of passive and active assistance designs in an occupational upper limb exoskeleton for overhead lifting. IISE Transactions on Occupational Ergonomics and Human Factors 9:167–185, DOI 10.1080/24725838.2021.1954565

8. Grieve JR, Dickerson CR (2008) Overhead work: Identification of evidence-based exposure guidelines. Occupational Ergonomics 8(1):53–66, DOI 10.3233/oer-2008-8105
9. Wang Z, Wu X, Zhang Y, Chen C, Liu S, Liu Y, Peng A, Ma Y (2021) A semi-active exoskeleton based on EMGs reduces muscle fatigue when squatting. Frontiers in Neurorobotics 15:30, DOI 10.3389/fnbot.2021.625479
10. Dunning KK, Davis KG, Cook C, Kotowski SE, Hamrick C, Jewell G, Lockey J (2010) Costs by industry and diagnosis among musculoskeletal claims in a state workers compensation system: 1999-2004. American Journal of Industrial Medicine 53(3):276–284, DOI 10.1002/ajim.20774
11. Blanchet L, Achiche S, Docquier Q, Fisette P, Raison M (2020) A procedure to optimize the geometric and dynamic designs of assistive upper limb exoskeletons. Multibody System Dynamics 51(2):221–245, DOI 10.1007/s11044-020-09766-6
12. de Looze MP, Bosch T, Krause F, Stadler KS, O'Sullivan LW (2016) Exoskeletons for industrial application and their potential effects on physical work load. Ergonomics 59(5):671–681, DOI 10.1080/00140139.2015.1081988
13. McFarland T, Fischer S (2019) Considerations for Industrial Use: A Systematic Review of the Impact of Active and Passive Upper Limb Exoskeletons on Physical Exposures. IISE Transactions on Occupational Ergonomics and Human Factors 7(3-4):322–347, DOI 10.1080/24725838.2019.1684399
14. Veale AJ, Xie SQ (2016) Towards compliant and wearable robotic orthoses: A review of current and emerging actuator technologies. Medical Engineering and Physics 38(4):317–325, DOI 10.1016/j.medengphy.2016.01.010
15. Nguiadem C, Raison M, Achiche S (2020) Motion planning of upper-limb exoskeleton robots: A review. Applied Sciences 10(21):1–21, DOI 10.3390/app10217626
16. Bougrinat Y, Achiche S, Raison M (2019) Design and development of a lightweight ankle exoskeleton for human walking augmentation. Mechatronics 64:102297, DOI 10.1016/j.mechatronics.2019.102297
17. Blanchet L, Achiche S, Docquier Q, Fisette P, Raison M (2021) A procedure to optimize the geometric and dynamic designs of assistive upper limb exoskeletons. Multibody System Dynamics 51(2):221–245, DOI 10.1007/s11044-020-09766-6
18. Miakovic L, Dezman M, Petric T (2022) Modular quasi-passive mechanism for energy storage applications: towards lightweight high-performance exoskeleton. In: Proceedings of the 20th International Conference on Advanced Robotics, IEEE, Ljubljana, Slovenia, pp 588–593, DOI 10.1109/icar53236.2021.9659353
19. Winter A, Mohajer N, Nahavandi D (2022) Semi-active assistive exoskeleton system for elbow joint. In: Proceedings of the IEEE International Conference on Systems, Man, and Cybernetics, IEEE, Melbourne, Australia, pp 2347–2353, DOI 10.1109/smc52423.2021.9658720
20. Nasr A, Ferguson S, McPhee J (2022) Model-based design and optimization of passive shoulder exoskeletons. Journal of Computational and Nonlinear Dynamics 17(5):051004, DOI 10.1115/1.4053405
21. Rahman T, Sample W, Seliktar R, Scavina MT, Clark AL, Moran K, Alexander MA (2007) Design and testing of a functional arm orthosis in patients with neuromuscular diseases. IEEE Transactions on Neural Systems and Rehabilitation Engineering 15(2):244–251, DOI 10.1109/TNSRE.2007.897026
22. Pehlivan AU, Celik O, O'Malley MK (2011) Mechanical design of a distal arm exoskeleton for stroke and spinal cord injury rehabilitation. In: Proceedings of the IEEE International Conference on Rehabilitation Robotics, IEEE, Zurich, Switzerland, pp 1–5, DOI 10.1109/ICORR.2011.5975428
23. Di Natali C, Sadeghi A, Mondini A, Bottenberg E, Hartigan B, De Eyto A, O'Sullivan LW, Rocon E, Stadler KS, Mazzolai B, Caldwell DG, Ortiz J (2020) Pneumatic quasi-passive actuation for soft assistive lower limbs exoskeleton. Frontiers in Neurorobotics 14:31, DOI 10.3389/fnbot.2020.00031
24. Otten A, Voort C, Stienen AH, Aarts R, Van Asseldonk E, Van Der Kooij H (2015) LIMPACT:A hydraulically powered self-aligning upper limb exoskeleton. IEEE/ASME Transactions on Mechatronics 20(5):2285–2298, DOI 10.1109/TMECH.2014.2375272
25. Altenburger R, Scherly D, Stadler KS (2016) Design of a passive, iso-elastic upper limb exoskeleton for gravity compensation. Robomech Journal 3(1):1–7, DOI 10.1186/s40648-016-0051-5
26. de Vries AW, de Looze MP (2019) The effect of arm support exoskeletons in realistic work activities : A review study. J Ergonomics 9(4):1–9, DOI 10.35248/2165-7556.19.9.255
27. Bogue R (2018) Exoskeletons – a review of industrial applications. Industrial Robot 45(5):585–590, DOI 10.1108/IR-05-2018-0109
28. Shank T, Eppes M, Hossain J, Gunn M, Rahman T (2017) Outcome measures with COPM of children using a Wilmington robotic exoskeleton. The Open Journal of Occupational Therapy 5(1):3, DOI 10.15453/2168-6408.1262
29. Luque EP, Högberg D, Iriondo A, Thorvald P (2019) Evaluation of the use of exoskeletons in the range of motion of workers. PhD thesis, University of Skovde, Skovde, DOI 10.1080/10255840008908000
30. Gopura RA, Bandara DS, Kiguchi K, Mann GK (2016) Developments in hardware systems of active upper-limb exoskeleton robots: A review. Robotics and Autonomous Systems 75:203–220, DOI 10.1016/j.robot.2015.10.001
31. Nasr A, Laschowski B, McPhee J (2021) Myoelectric control of robotic leg prostheses and exoskeletons: A review. In: Proceedings of the ASME International Design Engineering Technical Conferences and Computers and Information in Engineering Conference and Computers and Information in Engineering Conference, ASME, Online, Virtual, vol 85444, pp 2021–69203, DOI 10.1115/DETC2021-69203
32. Jamsek M, Petric T, Babix Jan (2020) Gaussian mixture models for control of quasi-passive spinal exoskeletons. Sensors 20(9):2705, DOI 10.3390/s20092705
33. Nasr A, Hashemi A, McPhee J (2022) Model-based mid-level regulation for assist-as-needed hierarchical control of wearable robots: A computational study of human-robot adaptation. Robotics 11(1):20, DOI 10.3390/robotics11010020
34. du Plessis T, Djouani K, Oosthuizen C (2021) A review of active hand exoskeletons for rehabilitation and assistance. Robotics 10(1):5351–5356, DOI 10.3390/robotics10010040
35. Sajadi MR, Nasr A, Moosavian SAA, Zohoor H (2015) Mechanical design, fabrication, kinematics and dynamics modeling, multiple impedance control of a wrist rehabilitation robot. In: Proceedings of the International Conference on Robotics and Mechatronics, IEEE, Tehran, Iran, pp 290–295, DOI 10.1109/ICRoM.2015.7367799
36. Gaudet G, Raison M, Achiche S (2021) Current trends and challenges in pediatric access to sensorless and sensor-based upper limb exoskeletons. Sensors 21(10), DOI 10.3390/s21103561
37. Kashiri N, Abate A, Abram SJ, Albu-Schaffer A, Clary PJ, Daley M, Faraji S, Furnemont R, Garabini M, Geyer H, Grabowski AM, Hurst J, Malzahn J, Mathijssen G, Remy D, Roozing W, Shahbazi M, Simha SN, Song JB, Smit-Anseeuw N, Stramigioli S, Vanderborght B, Yesilevskiy Y, Tsagarakis NG (2018) An overview on principles for energy efficient robot locomotion. Frontiers in Robotics and AI 5:129, DOI 10.3389/frobt.2018.00129

38. Al-Hayali NK, Nacy SM, Chiad JS, Hussein O (2021) Analysis and evaluation of a quasi-passive lower limb exoskeleton for gait rehabilitation. Al-Khwarizmi Engineering Journal 17(4):36–47, DOI 10.22153/kej.2021.12.007
39. Kh Al-Hayali N, Chiad JS, Nacy SM, Hussein O (2021) A review of passive and quasi-passive lower limb exoskeletons for gait rehabilitation. Journal of Mechanical Engineering Research and Developments 44(9):436–447
40. Matthew RP, Mica EJ, Meinhold W, Loeza JA, Tomizuka M, Bajcsy R (2015) Introduction and initial exploration of an active/passive exoskeleton framework for portable assistance. In: Proceedings of the IEEE International Conference on Intelligent Robots and Systems, IEEE, Hamburg, Germany, vol 2015-Decem, pp 5351–5356, DOI 10.1109/IROS.2015.7354133
41. Naito J, Nakayama A, Obinata G, Hase K (2007) Development of a wearable robot for assisting carpentry workers. International Journal of Advanced Robotic Systems 4(4):48, DOI doi.org/10.5772/5667
42. Otten BM, Weidner R, Argubi-Wollesen A (2018) Evaluation of a novel active exoskeleton for tasks at or above head level. IEEE Robotics and Automation Letters 3(3):2408–2415, DOI 10.1109/LRA.2018.2812905
43. Smith RL, Lobo-Prat J, Van Der Kooij H, Stienen AH (2013) Design of a perfect balance system for active upper-extremity exoskeletons. In: Proceedings of the IEEE International Conference on Rehabilitation Robotics, IEEE, Seattle, WA, USA, p 1–6, DOI 10.1109/ICORR.2013.6650376
44. Laschowski B, Razavian RS, McPhee J (2021) Simulation of stand-to-sit biomechanics for robotic exoskeletons and prostheses with energy regeneration. IEEE Transactions on Medical Robotics and Bionics 3(2):455–462, DOI 10.1109/TMRB.2021.3058323
45. Ren L, Cong M, Zhang W, Tan Y (2021) Harvesting the negative work of an active exoskeleton robot to extend its operating duration. Energy Conversion and Management 245:114640, DOI 10.1016/j.enconman.2021.114640
46. Hassan Z, Sadik W (2018) Design quasi passive exoskeleton for below knee prosthesis. Journal of Engineering and Applied Sciences 13(23):8994–9001
47. Lambrecht BG, Kazerooni H (2009) Design of a semi-active knee prosthesis. In: Proceedings of the IEEE International Conference on Robotics and Automation, IEEE, Kobe, Japan, pp 639–645, DOI 10.1109/ROBOT.2009.5152828
48. Pillai MV, Van Engelhoven L, Kazerooni H (2020) Evaluation of a lower leg support exoskeleton on floor and below hip height panel work. Human Factors 62(3):489–500, DOI 10.1177/0018720820907752
49. Bai S, Islam MR, Hansen K, Nørgaard J, Chen CY, Yang G (2022) A semi-active upper-body exoskeleton for motion assistance. Biosystems and Biorobotics 27:301–305, DOI 10.1007/978-3-030-69547-7{_}49
50. Zahedi A, Wang Y, Martinez-Hernandez U, Zhang D (2021) A wearable elbow exoskeleton for tremor suppression equipped with rotational semi-active actuator. Mechanical Systems and Signal Processing 157:107674, DOI 10.1016/j.ymssp.2021.107674
51. Inkol KA, McPhee J (2020) Assessing control of fixed-support balance recovery in wearable lower-limb exoskeletons using multibody dynamic modelling. In: Proceedings of the IEEE RAS and EMBS International Conference on Biomedical Robotics and Biomechatronics, IEEE, New York, NY, USA, pp 54–60, DOI 10.1109/BioRob49111.2020.9224430
52. Galinski D, Sapin J, Dehez B (2013) Optimal design of an alignment-free two-DOF rehabilitation robot for the shoulder complex. In: Proceedings of the IEEE International Conference on Rehabilitation Robotics, IEEE, Seattle, Washington, USA, pp 1–7, DOI 10.1109/ICORR.2013.6650502
53. Sarac M, Solazzi M, Sotgiu E, Bergamasco M, Frisoli A (2017) Design and kinematic optimization of a novel underactuated robotic hand exoskeleton. Meccanica 52(3):749–761, DOI 10.1007/s11012-016-0530-z
54. Manns P, Sreenivasa M, Millard M, Mombaur KD (2017) Motion optimization and parameter identification for a human and lower back exoskeleton model. IEEE Robotics and Automation Letters 2(3):1564–1570, DOI 10.1109/LRA.2017.2676355
55. Shi Y, Peng Q (2018) Improved benchmarking method using kinematics analysis in design of an upper limb exoskeleton rehabilitation device. In: Proceedings of the ASME International Design Engineering Technical Conferences and Computers and Information in Engineering Conference, ASME, Quebec City, Quebec, Canada, vol 4, p V004T05A001, DOI 10.1115/DETC2018-85465
56. Hayashi Y, Dubey R, Kiguchi K (2011) Torque optimization for a 7DOF upper-limb power-assist exoskeleton robot. In: Proceedings of the IEEE Workshop on Robotic Intelligence In Informationally Structured Space, IEEE, Paris, France, pp 49–54, DOI 10.1109/RIISS.2011.5945786
57. Marinou GD, Mombaur KD (2022) Optimizing active spinal exoskeletons to minimize low back loads. Biosystems and Biorobotics 27:455–460, DOI 10.1007/978-3-030-69547-7{_}73
58. Aoustin Y, Formalskii AM (2018) Walking of biped with passive exoskeleton: evaluation of energy consumption. Multibody System Dynamics 43(1):71–96, DOI 10.1007/s11044-017-9602-7
59. Harbauer CM, Fleischer M, Bandmann CE, Bengler K (2022) Optimizing force transfer in a soft exoskeleton using biomechanical modeling. In: Proceedings of the 21st Congress of the International Ergonomics Association, Springer, Vancouver, BC, Canada, vol 223, pp 274–281, DOI 10.1007/978-3-030-74614-8{_}33
60. Zhou L, Li Y, Bai S (2017) A human-centered design optimization approach for robotic exoskeletons through biomechanical simulation. Robotics and Autonomous Systems 91:337–347, DOI 10.1016/j.robot.2016.12.012
61. Park D, Cho KJ (2017) Development and evaluation of a soft wearable weight support device for reducing muscle fatigue on shoulder. PLoS ONE 12(3):e0173730, DOI 10.1371/journal.pone.0173730
62. Mehrabi N, Razavian RS, Ghannadi B, McPhee J (2017) Predictive simulation of reaching moving targets using nonlinear model predictive control. Frontiers in Computational Neuroscience 10:143, DOI 10.3389/fncom.2016.00143
63. Mallat R, Khalil M, Venture G, Bonnet V, Mohammed S (2019) Human-Exoskeleton Joint Misalignment: A Systematic Review. In: International Conference on Advances in Biomedical Engineering, ICABME, IEEE, Tripoli, Lebanon, vol 2019-Octob, pp 1–4, DOI 10.1109/ICABME47164.2019.8940321
64. Panero E, Muscolo GG, Gastaldi L, Pastorelli S (2020) Multibody analysis of a 3D human model with trunk exoskeleton for industrial applications. Computational Methods in Applied Sciences 53:43–51, DOI 10.1007/978-3-030-23132-3{_}6
65. Cortes C, De Los Reyes-Guzman A, Scorza D, Bertelsen A, Carrasco E, Gil-Agudo A, Ruiz-Salguero O, Florez J (2016) Inverse kinematics for upper limb compound movement estimation in exoskeleton-assisted rehabilitation. BioMed Research International 2016:1–14, DOI 10.1155/2016/2581924
66. Laitenberger M, Raison M, Périé D, Begon M (2015) Refinement of the upper limb joint kinematics and dynamics using a subject-specific closed-loop forearm model. Multibody System Dynamics 33(4):413–438, DOI 10.1007/s11044-014-9421-z
67. Nasr A, Bell S, He J, Whittaker RL, Jiang N, Dickerson CR, McPhee J (2021) MuscleNET: Mapping electromyography to kinematic and dynamic biomechanical variables. Journal of Neural Engineering 18(4):0460d3, DOI

10.1088/1741-2552/ac1adc
68. Nasr A, McPhee J (2022) Biarticular MuscleNET: A machine learning model of biarticular muscles. In: Proceedings of the North American Congress on Biomechanics, Ottawa, Canada
69. Alabdulkarim S, Nussbaum MA (2019) Influences of different exoskeleton designs and tool mass on physical demands and performance in a simulated overhead drilling task. Applied Ergonomics 74:55–66, DOI 10.1016/j.apergo.2018.08.004
70. Grazi L, Trigili E, Proface G, Giovacchini F, Crea S, Vitiello N (2020) Design and experimental evaluation of a semi-passive upper-limb exoskeleton for workers with motorized tuning of assistance. IEEE Transactions on Neural Systems and Rehabilitation Engineering 28(10):2276–2285, DOI 10.1109/TNSRE.2020.3014408
71. Kim S, Nussbaum MA (2019) A follow-up study of the effects of an arm support exoskeleton on physical demands and task performance during simulated overhead work. IISE Transactions on Occupational Ergonomics and Human Factors 7(3-4):163–174, DOI 10.1080/24725838.2018.1551255
72. Kim S, Nussbaum MA, Mokhlespour Esfahani MI, Alemi MM, Jia B, Rashedi E (2018) Assessing the influence of a passive, upper extremity exoskeletal vest for tasks requiring arm elevation: Part II – "Unexpected" effects on shoulder motion, balance, and spine loading. Applied Ergonomics 70:323–330, DOI 10.1016/j.apergo.2018.02.024
73. Ackermann M, van den Bogert AJ (2010) Optimality principles for model-based prediction of human gait. Journal of Biomechanics 43(6):1055–1060, DOI 10.1016/j.jbiomech.2009.12.012
74. Theurel J, Desbrosses K, Roux T, Savescu A (2018) Physiological consequences of using an upper limb exoskeleton during manual handling tasks. Applied Ergonomics 67:211–217, DOI 10.1016/j.apergo.2017.10.008
75. Liu ZH, Qiu YX, Zhu ZH, Zhou YW, Tang Z (2016) Effects of memory foam on optimizing shoulder fatigue of wearable exoskeleton. Journal of Donghua University (English Edition) 33(4):536–539
76. Liu S, Hemming D, Luo RB, Reynolds J, Delong JC, Sandler BJ, Jacobsen GR, Horgan S (2018) Solving the surgeon ergonomic crisis with surgical exosuit. Surgical Endoscopy 32(1):236–244, DOI 10.1007/s00464-017-5667-x
77. Nasr A, Inkol KA, Bell S, McPhee J (2021) InverseMuscleNET: Alternative machine learning solution to static optimization and inverse muscle modelling. Frontiers in Computational Neuroscience 15:759489, DOI 10.3389/fncom.2021.759489
78. Inkol KA, Brown C, McNally W, Jansen C, McPhee J (2020) Muscle torque generators in multibody dynamic simulations of optimal sports performance. Multibody System Dynamics 50(4):435–452, DOI 10.1007/s11044-020-09747-9
79. Ghannadi B, Mehrabi N, Razavian RS, McPhee J (2017) Nonlinear model predictive control of an upper extremity rehabilitation robot using a two-dimensional human-robot interaction model. In: Proceedings of the IEEE International Conference on Intelligent Robots and Systems, IEEE, Vancouver, BC, Canada, vol 2017-Septe, pp 502–507, DOI 10.1109/IROS.2017.8202200
80. Mombaur KD, Clever D (2017) Inverse optimal control as a tool to understand human movement. In: Laumond JP, , Mansard N, , Lasserre JB (eds) Geometric and numerical foundations of movements, vol 117, Springer, pp 163–186, DOI 10.1007/978-3-319-51547-2{_}8
81. Reinkensmeyer DJ, Wynne JH, Harkema SJ (2002) A robotic tool for studying locomotor adaptation and rehabilitation. In: Proceedings of the Annual International Conference of the IEEE Engineering in Medicine and Biology, IEEE, Houston, TX, USA, vol 3, pp 2353–2354, DOI 10.1109/iembs.2002.1053318
82. Dumas R, Chèze L, Verriest JP (2007) Adjustments to McConville et al. and Young et al. body segment inertial parameters. Journal of Biomechanics 40(3):543–553, DOI 10.1016/j.jbiomech.2006.02.013
83. Yamaguchi GT (2006) Dynamic modeling of musculoskeletal motion: A vectorized approach for biomechanical analysis in three dimensions, 1st edn. Springer, Boston, MA, USA, DOI 10.1007/978-0-387-28750-8
84. Angold R, Lubin J, Solano M, Paretich C, Mastaler T (2016) Exoskeleton and method of providing an assistive torque to an arm of a wearer
85. Gopura RA, Kiguchi K, Bandara DS (2011) A brief review on upper extremity robotic exoskeleton systems. In: Proceedings of the 6th International Conference on Industrial and Information Systems, IEEE, Kandy, Sri Lanka, pp 346–351, DOI 10.1109/ICHNFS.2011.6038092
86. Hunter I, Ballantyne J, Hollerbach JM (1991) A comparative analysis of actuator technologies for robotics. Robotics Review 2:299–342
87. García PL, Crispel S, Saerens E, Verstraten T, Lefeber D (2020) Compact gearboxes for modern robotics: A review. Frontiers in Robotics and AI 7:103, DOI 10.3389/frobt.2020.00103
88. Seok S, Wang A, Chuah MY, Hyun DJ, Lee J, Otten DM, Lang JH, Kim S (2015) Design principles for energy-efficient legged locomotion and implementation on the MIT Cheetah robot. IEEE/ASME Transactions on Mechatronics 20(3):1117–1129, DOI 10.1109/TMECH.2014.2339013
89. Wensing PM, Wang A, Seok S, Otten DM, Lang J, Kim S (2017) Proprioceptive actuator design in the MIT cheetah: Impact mitigation and high-bandwidth physical interaction for dynamic legged robots. IEEE Transactions on Robotics 33(3):509–522, DOI 10.1109/TRO.2016.2640183
90. Hughes A, Drury B (2019) Electric Motors and Drives: Fundamentals, Types and Applications. Elsevier, DOI 10.1016/B978-0-08-102615-1.09989-X
91. Inkol KA, McPhee J (2021) Towards compliant human-exoskeleton interactions within multibody dynamics simulations of assisted human motor control. In: ECCOMAS Thematic Conference on Multibody Dynamics, Budapest, Hungary
92. Jarrasse N, Morel G (2012) Connecting a human limb to an exoskeleton. IEEE Transactions on Robotics 28(3):697–709, DOI 10.1109/TRO.2011.2178151
93. Stienen AH, Hekman EE, van der Helm FC, van der Kooij H (2009) Self-aligning exoskeleton axes through decoupling of joint rotations and translations. IEEE Transactions on Robotics 25(3):628–633, DOI 10.1109/TRO.2009.2019147
94. Gull MA, Bai S, Bak T (2020) A review on design of upper limb exoskeletons. Robotics 9(1):16, DOI 10.3390/robotics9010016
95. Anderson DE, Madigan ML, Nussbaum MA (2007) Maximum voluntary joint torque as a function of joint angle and angular velocity: Model development and application to the lower limb. Journal of Biomechanics 40(14):3105–3113, DOI 10.1016/j.jbiomech.2007.03.022
96. Kim JH, Roberts D (2015) A joint-space numerical model of metabolic energy expenditure for human multibody dynamic system. International Journal for Numerical Methods in Biomedical Engineering 31(9):e02721, DOI 10.1002/cnm.2721
97. Laschowski B, McPhee J, Andrysek J (2019) Lower-Limb Prostheses and Exoskeletons With Energy Regeneration: Mechatronic Design and Optimization Review. Journal of Mechanisms and Robotics 11(4):040801, DOI 10.1115/1.4043460